12

Deformation in the Presence of Fluids and Mineral Reactions

Effect of Fracturing and Fluid–Rock Interaction on Seismic Cycles

JEAN-PIERRE GRATIER[1] and FRÉDÉRIC GUEYDAN[2]

[1]LGIT, CNRS-Observatoire, Geosciences, Rue de la Piscine,
Université Joseph Fourier, 38041 Grenoble, France
[2]Geosciences Rennes, Université Rennes 1, Bat. 15, Campus de Beaulieu,
35042 Rennes, France

ABSTRACT

Natural and experimental deformation of fault rocks show that fluid flow and mineral reactions are linked to fracturing in a nonlinear feedback relationship that potentially affects the displacement and stress histories of large faults. These interactions spawn instabilities that are expressed as episodic seismic events involving cataclasis, which alternate with slow, aseismic deformation involving pressure-solution creep, as well as healing and sealing by fluid-assisted mass transfer. This chapter focuses on the timescale of these processes during the earthquake cycle, with special emphasis on the evolution of rheological and transport properties of fault rock during the interseismic period. Fracturing weakens faults dramatically by enhancing the kinetics of pressure-solution creep and of mineral reactions. Therefore, during the postseismic period and initial part of the interseismic period, weakening is faster than fault strengthening by healing and sealing of fractures. During the interseismic period, mass transfer associated with fluid-assisted chemical reactions smoothes asperities on fault surfaces, heals fractures and enhances the formation of a foliation parallel to the fault plane, and decreases permeability. If advective fluid inflow is significant, this can increase pore-fluid pressure and reduce effective shear strength, at least locally within the fault. In the long term, however, the combined effect of fracturing, pressure-solution creep, and sealing is to restore the rheological and transport properties of the fault during the interseismic period, setting the

stage for renewed stress build-up and seismicity. We demonstrate the salient characteristics of fluid-assisted fault weakening and strengthening with a one-dimensional model of an idealized fault zone undergoing simple shear at constant velocity. The model shows that the kinetics of the weakening and strengthening processes determine the relative rates of shear stress decrease and increase during the interseismic period. The kinetics of dissolution precipitation and mineral reactions are therefore expected to exert an important control on the recurrence time of earthquakes.

INTRODUCTION

Several lines of evidence show that fluids play a key role in the dynamics of faulting. Fluids are preserved within inclusions in minerals that grew in fault zones. The isotopic composition of such fluids reveals various origins: meteoric fluids and metamorphic fluids produced by chemical reactions in the lower crust or mantle (Hickman et al. 1995). In some cases, cyclical fault cementation (e.g., Stel 1981) betrays transient flow along paths which episodically opened by critical fracturing and closed by crystal growth and compaction processes. The presence of reactive fluids is also crucial in accommodating deformation by mass transfer in solution. Pressure solution is the main mechanism competing with cataclasis in the upper crust (Figure 12.1a).

Both mechanisms are well documented in exhumed natural fault rocks. In the upper crust, deformation accommodated by mass transfer in a solution does not require high differential stresses. However, chemical reactions in a nonhydrostatic stress field are generally very slow, resulting in strain rates ranging from 10^{-11} to 10^{-15} s^{-1} (Rutter 1976; Pfiffner and Ramsay 1982). Reproducing such low strain rates in the presence of a fluid in the laboratory is therefore a challenge (Paterson 2001). In contrast, cataclasis can be very fast (strain rates of 10^{-2} to 10^{0} s^{-1}). Such rates are reproducible in the lab, but require much higher differential stresses. Neither mechanism is very sensitive to temperature; they tend to become subordinate to thermally activated creep at depths greater than 10–15 km (Figure 12.1a).

Cataclasis and deformation by diffusive mass transfer are not mutually independent processes. Their interaction leads to complex behavior both in time and in space. Both mechanisms affect weakening and strengthening, but their characteristic times are very different (Chapter 4). It is convenient to distinguish three characteristic times for the evolution of the mechanical properties of fault rocks:

Seconds to minutes are characteristic of cataclastic failure associated with earthquakes. The role of fluids during such short intervals is mostly mechanical (due to change of fluid pressure associated with fluid advection) or catalytic (melting).

Tens to thousands of years is characteristic for the evolution of the rheological and transport properties of rock during the interseismic period (Chapter 7).

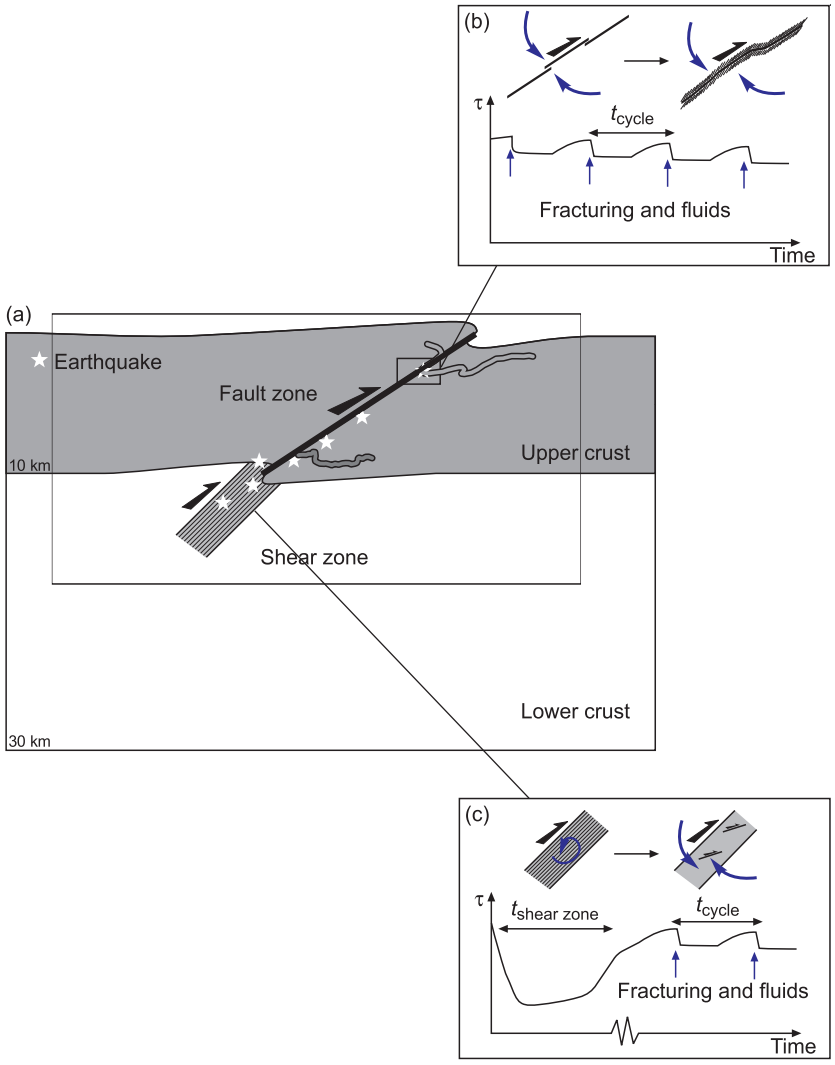

Figure 12.1 Schematic view of seismic and aseismic interactions within the crust. (a) Cataclastic, seismic faulting in the upper crust competes with aseismic deformation (folding, cleavage formation) associated with diffusive mass transfer (pressure solution, mineral reactions). In the lower crust, mostly aseismic deformation (predominantly by dislocation creep, diffusion creep) may be associated with rare earthquakes due to subordinate cataclasis. (b) Individual fault strands in the upper crust coalesce to form mature fault zone networks during successive cycles (stars) and associated inflow of fluids and stress changes (τ). (c) Shear zone networks in the lower crust evolve over longer times, initially in a closed system for fluids. Coseismic ruptures propagate downward into the lower crust, creating pathways for the downward flow of fluids.

In this chapter, we focus on the role of fracturing and fluid–rock interactions within this time interval because these processes are key in the weakening and strengthening of faults in the upper crust. In the following, we show how fracturing speeds up the kinetics of pressure-solution creep and mineral reaction, leading to dramatic weakening as well as to progressive healing and strengthening of faults. To demonstrate these effects we present some simple models which explain how the duration of the interseismic period, and thus the recurrence time of large earthquakes, is directly related to the kinetics of fluid–rock interaction.

Thousand to millions of years is the characteristic time of chemical and mechanical differentiation processes associated with mass transfer (e.g., Robin 1979). The deformation of natural polymineralic rocks leads to chemical and mechanical differentiation at all scales, from a few microns to several kilometers (Gratier 1987). For example, fault zones develop into narrow weak gouge between progressively strengthened damage zones (Figure 12.1b; e.g., Evans and Chester 1995). Long-term weakening associated with reactive mass transfer (Wintsch et al. 1995) is also responsible for the formation of ductile shear zones (Figure 12.1c). The duration of strain localization in ductile shear zones is crudely estimated to range anywhere from a few thousand years (Handy 1989) to tens of millions years (Muller et al. 2000). Placing tighter constraints on the rates of weakening and localization awaits the development of new analytical techniques to date fabric associated with syn-tectonic mineralization events (Chapter 14).

FRACTURING AND FLUID–ROCK INTERACTIONS

Basic Concepts

Thermodynamics: The Driving Forces

Stress affects the chemical potential of a solid by increasing both its molar free energy and surface chemical potential compared to that at zero stress (Gibbs 1877; Paterson 1973). Though Gibbs free energy is not defined for a nonhydrostatically stressed solid, dissolution and precipitation of a solid is commonly described by the surface chemical potential:

$$\Delta\mu = \Delta f + V_s \Delta\sigma_n + \Delta E_s \qquad (12.1)$$

where μ is the chemical potential of the dissolved component, σ_n is the normal stress or the fluid pressure P on the solid, f is the molar Helmholtz free energy, V_s is the molar volume of the solid, E_s is the surface energy $\gamma V_s\,(1/r + 1R)$, with γ interfacial energy, and r and R are the principal radii of curvature (Kingery et al. 1976). Equation 12.1 characterizes the chemical potential of the solid at each point on the mineral surface. This potential is a function of the normal

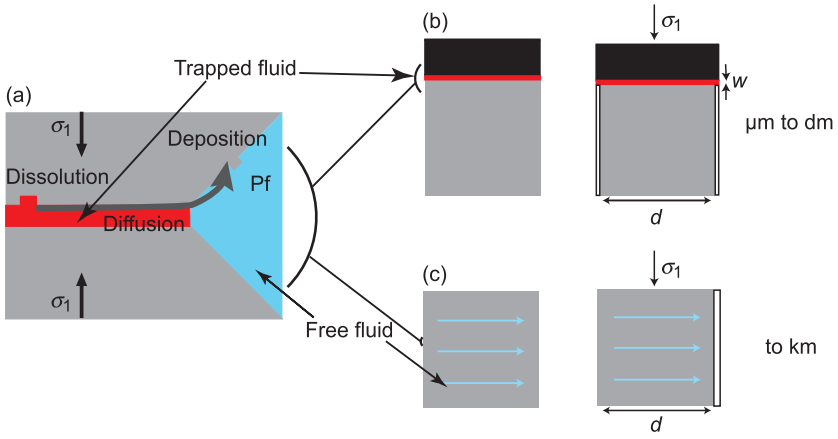

Figure 12.2 Basic concepts of pressure-solution creep: (a) Dissolution at contact between continuous or discontinuous fluid phases and stressed solids, oriented normal to normal to σ_1; the dissolved species are transferred by diffusion within this trapped fluid and re-deposited on the free surfaces of the solid at fluid pressure, P_f, or possibly on any surfaces in contact with the fluid and at normal stress less than σ_1. Various creep models are possible depending on the rate-limiting step of this process and on the mechanism of mass transfer. (b) Diffusion along the boundaries of the solid driven by a chemical potential gradient; (c) fluid advection through the solid driven by head gradient $\Delta h / \Delta x$.

stress, which varies from the contact surface (σ_n) to the pore surface (P_f) in Figure 12.2a. The driving force for material transfer along a grain surface is therefore the difference in chemical potentials at the stressed and un- or less-stressed surfaces. The term Δf contains various contributions (Paterson 1973):

$$\Delta f = \Delta E_e + \Delta E_p \tag{12.2}$$

where E_e is the elastic strain energy, and E_p is the plastic strain energy due to dislocations.

The driving force linked to the difference of surface curvature ΔE_s, sometimes called the coarsening potential (Ostwall ripening), includes both the effect of the small particles trapped in the crack and the change in surface curvature of the crack (including changes induced by crack healing). The effect of the difference in normal stresses is most often one or two orders of magnitude greater that of other effects (Paterson 1973; Lehner 1995; Shimizu 1995). However, in cases when the normal stress does not vary along the solid surface (e.g., in cavities under pressure), each of the contributions to Δf and ΔE_s may drive mass transfer. For example, ΔE_s is the driving force associated with self-healing of the crack (Brantley et al. 1990), ΔE_e and/or ΔE_p are responsible for local dissolution near the boundary of an indenter (Tada and Siever 1986).

Kinetics: The Limiting Processes

Pressure solution is a sequence of three processes: dissolution, mass transfer, and deposition. The slowest of these processes imposes its kinetics on the whole deformation process and is termed the rate-limiting step or process. Various creep equations may be written according to which process is rate-limiting, an approach which we have summarized briefly below. However, when the kinetics in of the three processes is very similar, the driving force is partitioned subequally between these processes, leading to a relatively complex equation (Raj 1982).

Mass transfer in nature may occur both by diffusion and by advection, although generally advective fluid flow is more competitive at longer length scales (m to km), as discussed in 'Chapter 11. In this chapter we do not consider in detail the various creep laws based on the assumptions above (e.g., Paterson 2001). If the only driving force for pressure solution is the difference in normal stress between contacting and free surfaces, then creep laws for the deformation of a rock cube in a closed system take the form of the following equations:

(R) $$\dot{\varepsilon} = \alpha k c V_s (\Delta\sigma_n)^n / RTd \tag{12.3}$$

if dissolution or crystallization are the rate-limiting processes (Raj 1982)

(D) $$\dot{\varepsilon} = \beta D w c V_s (\Delta\sigma_n)^n / RTd^3 \tag{12.4}$$

if diffusion through a stressed fluid phase is the rate-limiting process (Rutter 1976) and

(I) $$\dot{\varepsilon} = \lambda K \Delta c \Delta h / \Delta x d \tag{12.5}$$

if advection through a porous aggregate is the rate-limiting process (Gratier and Gamond 1990).

In all three equations above, $\dot{\varepsilon}$ is the axial strain rate ($\Delta d/d\Delta t$), α, β, and λ are dimensionless constants that depend on the geometry of the interface, d is the length of one side of the deforming cube and corresponds to the size of the closed system for mass transfer (Figure 12.2b, model R and D; Figure 12.2c, model R and I), t is time, k is the rate of reaction, c is the concentration of solid in solution (models R and D, volumetric ratio), V_s is the molar volume of the stressed solid, and Δc (model I and Figure 12.2c) is the difference in concentration of the solid in solution between the zone of dissolution (fluid–mineral interaction through the entire cube of rock) and the zone of deposition (sealed fracture). R is the gas constant, T is temperature in K, K is the permeability coefficient, and $\Delta h/\Delta x$ is the head gradient that drives advective transport.

Three principal models can describe the stressed fluid phase: (a) the thin-fluid film model (Weyl 1959; Rutter 1976); (b) the island-channel model (Raj 1982; Spiers and Schutjens 1990); and (c) the microcracking model (Gratz 1991;

den Brok 1998). Here, we consider a thin-fluid model with diffusion coefficient, D, and thickness of the fluid phase, w, subjected to normal stress, σ_n. The stress exponent, n, is 1 in most pressure-solution creep laws. However, for several reasons this is only true to a first approximation:

- The difference in solubility of the solid between the zone of dissolution and the zone of deposition depends exponentially on the chemical potential (Dewers and Ortoleva 1990).
- When diffusion is rate-controlling and maintains the balance of the diffusive flux out of the fluid film, the normal stress at the center of the contact must be higher than the average stress across the contact (Weyl 1959; Rutter 1976). In this situation, a stress exponent of 1 is only predicted at differential stress values of $\Delta\sigma_n$ less than 30 MPa.
- When dissolution or precipitation is rate-controlling, n reflects the magnitude of the interface velocity versus the driving force relation and is typically 2 for spiral growth/dissolution (two-dimensional nucleation or dissolution on surfaces that are smooth and flat on the atomic scale) and 1 for a rough interface (evolution without a layer-to-layer mechanism of growth or dissolution; Niemeijer and Spiers 2002). Indentation experiments on quartz (Figure 12.3a) confirm this complex nonlinear behavior. For example, an experimental curve $\Delta l/\Delta t = f(\Delta\sigma_n)^n$ can be fitted by a power law with n ranging from 1.3 to 2 (Gratier, unpublished results).

Other creep laws are possible, with each step potentially rate-limiting. Crystallization must also be considered as a possible rate-limiting process, either due to coating of the depositional surface or to the small surface area available for precipitation. In the latter case, crystallization must occur under stress. This is the so-called "force of crystallization" concept that was verified experimentally by Taber (1916) and has rarely been discussed since (Weyl 1959; Means and Li 2001; Hilgers et al. 2004).

The creep laws in Eqs. 12.3, 12.4, and 12.5 operate over a large range of conditions. The most important parameters controlling the relative activity of the mechanisms in these models are strain rate, size of the closed system, and temperature and nature of solids and fluids. For example, pressure solution of quartz is controlled by reaction rate at low temperature and by diffusion rate at high temperature (Oelkers et al. 1996; Renard et al. 1997). The nature of solids and fluids is also a key factor. For example, impurity ions in the pore fluid can slow the reaction rate (Zhang et al. 2002) and consequently control mass transfer rates in some natural systems. Special attention should be paid to the relationship between strain rate, $\dot{\varepsilon}$ and the size of the closed system, d, which varies from $1/d$ for the I and R laws, to $1/d^3$ for the D law. The size of the closed system also varies with the mass transfer process: micrometer to decimeter for diffusion transfer (model D) compared to hundreds to thousands of meters for advective transfer (model I, see also Chapter 11).

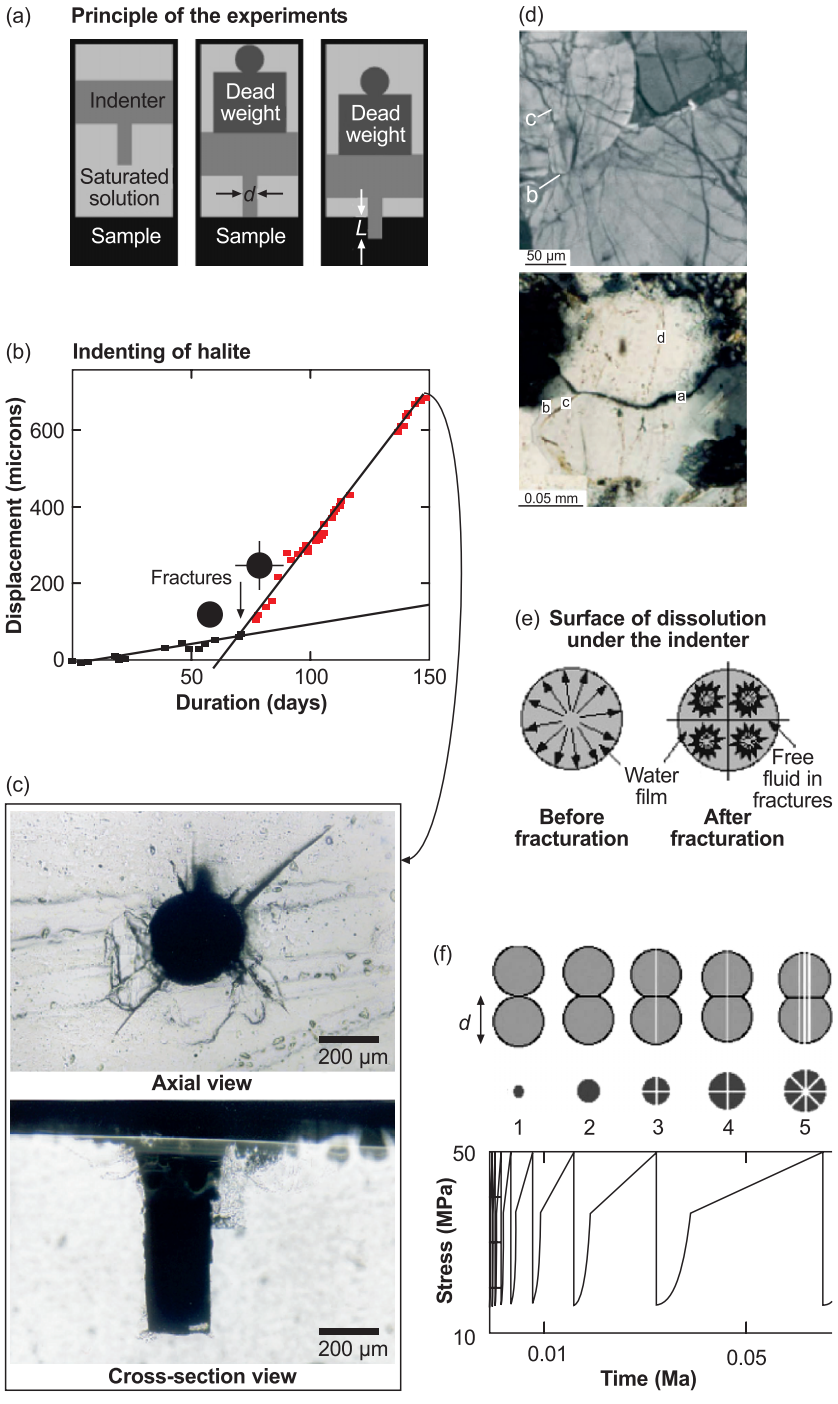
(a) Principle of the experiments
Indenter
Saturated solution
Sample
Dead weight
d
Sample
Dead weight
L
(b) Indenting of halite
Displacement (microns)
600
400
200
0
Fractures
50
100
150
Duration (days)
(c)
200 µm
Axial view
200 µm
Cross-section view
(d)
c
b
50 µm
d
b
c
a
0.05 mm
(e) Surface of dissolution under the indenter
Water film
Free fluid in fractures
Before fracturation
After fracturation
(f)
d
1
2
3
4
5
50
Stress (MPa)
10
0.01
0.05
Time (Ma)

Evaluating the validity of the creep laws above under natural conditions is not easy. The characteristic times for diffusion, transport, and precipitation on a given length scale are several orders of magnitude longer than the human life span. Therefore, the kinetics of these processes in the laboratory must be accelerated so that experimentalists can outlive their experiments. This can be achieved in one of several ways, each with its attendant problems:

- Solubility can be increased, but not without inducing possible chemical side effects.
- Temperature can be increased but only at the risk of favoring solid-state creep mechanisms with a higher activation energy than that of pressure solution (e.g., Nabarro-Herring creep, a mechanism that is otherwise unlikely to operate in fault rocks, Rutter 1983).
- Stress can be increased at the risk of inducing intracrystalline plasticity (dislocation glide plus climb) or cataclasis.

Taken together, these problems raise the question of how to model the rheological behavior of large volumes of rock with constitutive equations that are derived only from laboratory specimens at unnaturally high strain rates. Possible solutions to the problem of scaling are discussed by Paterson (2001) and touched on in Chapter 1.

Observations from both experiments and nature show that microfracturing of minerals can drastically increase the kinetics of pressure solution. Because microfracturing occurs suddenly, pressure solution favors transient creep.

Evidence from Experiments

In the experimental set-up in Figure 12.3a, a stainless steel cylindrical indenter is mounted beneath a Teflon piston in contact with a crystal of halite in its brine. Before the indenter is placed in contact with the sample, the crystal is immersed in brine that was previously saturated with halite powder at the temperature of the experiment. This is done to trap a saturated fluid phase beneath

◂ **Figure 12.3** Effect of fracturing on the kinetics of pressure-solution creep. (a) Configuration of the indenter experiment; (b) Displacement of indenter in halite with time (note the drastic increase of displacement rate associated with radial fracturing at day 71). (c) Axial view (top) and cross-sectional view (bottom) of the radial fractures that developed on day 71. (d) Natural fractures at the contact between two stressed solids that underwent pressure-solution indentation; (e) Axial view showing reduction of mean distance of diffusive mass transfer within trapped fluids from (d) (before fracturing) to less than $d/2$ (after fracturing). (f) Unstable behavior caused by competition of fracturing and fracture-induced increase in dissolution surface when diffusion is rate-limiting at constant displacement rate (adapted from Gratier et al. 1999).

the indenter before the indenter exerts stress. In this example, the dead weight induces a stress of about 16 MPa on the indenter. The device was maintained at a temperature of 25°C. For the 150-day duration of the experiment, the displacement of the indenter was registered by following a reference line on the piston under a microscope (Figure 12.3b). The result was rather surprising: the displacement rate of the indenter was constant for the first 71 days (less than 1 micron per day) before suddenly accelerating by a factor of 8. This increased displacement rate persisted for the remaining 77 days of the experiment. After the sample was polished, the depth of the hole created by dissolution of the halite beneath the indenter matched the measured displacement (Figure 12.3c). Other than this cylindrical hole, the only change in the structure of the sample occurred on day 71, when the displacement rate suddenly increased and radial fractures developed in the halite beneath the indenter, as seen in Figure 12.3c. Previous experiments conducted with a similar set-up (Hickman and Evans 1991, 1995; de Meer et al. 2002; Dysthe et al. 2003) did not show any fractures developed during indentation.

The effect of fracturing on the displacement rate in our experiments is obvious and irreversible. We interpreted fracturing to have augmented the rate of diffusive mass transfer along the contact between the indenter and halite (Gratier et al. 1999). Without fracturing, the displacement rate ($\Delta d/\Delta t$) is controlled by the rate of mass transfer out of the thin-fluid film trapped beneath the indenter, and is inversely proportional to the square of the diameter, d, of the indenter (model D, Eq. 12.4). Within this trapped fluid phase (Figure 12.3b, before fracturing), the product Dw ($m^3\ s^{-1}$) is about $5 \times 10^{-19}\ m^3\ s^{-1}$, which is in good agreement with values from previous work (Hickman and Evans 1995; de Meer et al. 2002). Radial fractures that are longer than the diameter of the indenter and several microns wide form paths filled with a free fluid that facilitates the fast removal of material away from the contact area. There, the product of the diffusion coefficient ($2 \times 10^{-9}\ m^2\ s^{-1}$) and the width of the mass transfer path (2×10^{-6} m) is about $4 \times 10^{-15}\ m^3\ s^{-1}$, that is, about 8×10^3 higher than within the thin-fluid phase otherwise trapped beneath the indenter. After fracturing, the initially thin-fluid film is distributed among several smaller domains, with each domain bounded by fast diffusive paths (Figure 12.3e). Therefore, fracturing renders the displacement rate inversely proportional to the square of the mean size of the small domains bounded by the radial fractures. This explains the sudden increase of the displacement rate, as pressure-solution indentation is diffusion controlled. The ratio between the indenter diameter and the mean size of the fractured domains is about 2.8.

A significant increase in the rate of pressure solution was previously attributed to subcritical microcrack growth (Gratz 1991; den Brok 1998) at grain boundaries, where channels along closely spaced microcracks intersect the dissolution surface. The location of these channels changes continuously as

microcracking progresses (dynamic channel island model). Therefore, microcracking and its effects on diffusivity were considered to be integral parts of steady-state pressure-solution creep.

In contrast, we propose that creep is unsteady, because fracturing is able to connect the fluid phase under stress with the free fluid located around the contact. This short cut in the diffusional mass transfer path is responsible for the sudden increase of the creep rate. We suggest that transgranular fracturing during earthquakes drastically enhances pressure solution and weakens rocks after seismic events.

Fluid-filled microfractures that potentially act as shortcuts in the diffusional path have also been proposed to account for high rates of measured diffusion (Farver and Yund 1998). However, fast healing may alleviate such shortcuts. Note that at the conditions of our experiment the fractures do not heal, but remain open paths of fast diffusion throughout the experiment. However, healing and sealing are very common processes in both experimental and natural deformation, and strength recovery is a key process that competes with dissolution. This will be discussed in the following section in the context of fault healing and strengthening.

Applications to Nature

Fractured Grains or Pebbles

The idea that fracturing enhances pressure solution has several applications in natural deformation. Pitted pebbles have long been attributed to pressure solution (Sorby 1865; McEwen 1978, Figure 12.3d). However, the large size of the dissolution areas (cm) is incompatible with the known duration of deformation and is certainly inconsistent with experimentally derived parameters for pressure solution. Only the development of fractures at stressed contacts explains the relatively high strain rate inferred for the large pits. A numerical model of the complex interaction between pressure solution and fracturing (Gratier et al. 1999) explains why these two mechanisms are so often associated in nature. For example, a cyclic stress-time function at constant displacement rate is derived by taking into account the ratio of stress to the diameter of dissolution (σ/d^2). Without any fracture, the contact area increases and stress must increase in order to maintain a constant displacement rate. However, stress cannot increase infinitely, otherwise the pebble will fracture. If fracturing does occur, then the dissolution contact area is broken up into smaller domains, reducing the mean distance of diffusion that controls the kinetics of mass transfer (Figure 12.3f). Therefore, the stress needed to maintain a constant displacement rate is drastically reduced. This model yields a mean viscosity of 3×10^{21} Pa s, but the viscosity and the stress values evolve with time (Figure 12.3f).

Fracturing and Reaction Weakening

Reaction weakening involves the nucleation and growth of reaction products that are weaker than the reactants. Reaction weakening assisted by micro-fracturing and diffusive mass transport in fluids is common during shear zone formation in the lithosphere (Wintsch et al. 1995; Handy and Stunitz 2002). Fracturing creates the space necessary for the infiltration of fluids that are required for the reaction to take place. Figure 12.4 shows three examples described below:

1. Midcrustal shear zones often consist of fine-grained mylonites within granitoid host rocks, typical of continental crust (FitzGerald and Stünitz 1993). At greenschist-facies conditions (depths of 10–20 km), quartz deforms predominantly by dislocation creep while feldspar fractures (Simpson 1985). The transformation of feldspar to very fine-grained white mica, albite, and clinozoisite is inferred to weaken the rocks (e.g., Mitra 1978; White and Knipe 1978; Dixon and Williams 1983; Gapais 1989; Wibberley 1999). Coeval syntectonic feldspar fracturing and reaction weakening within the Tenda Shear Zone of eastern Corsica (Gueydan et al. 2003; Figure 12.4) affected granitoids that can be considered as homogeneous at the regional scale. The modal amount of white mica increases with strain and reaches a maximum value of 50%. At midcrustal depths, the transformation of feldspar to white mica requires the addition of water. The formation of fine-grained white mica weakens the material and so favors strain localization, ultimately within meter- to kilometer-wide shear zones.
2. Handy and Stünitz (2002) showed that fracturing and reaction weakening are responsible for the formation of shear zones in the upper part of the lithospheric mantle during Early Mesozoic rifting of the Apulian continental margin. During extensional unroofing of these mantle rocks, fracturing triggered the progressive replacement of olivine, clinopyroxene, orthopyroxene, and spinel by a hydrous, lower-pressure assemblage of olivine, plagioclase, and hornblende. This reaction, which required fracturing and fluids, weakened the material by at least an order of magnitude (stage 1, Figure 12.4) as inferred from microstructural evidence for viscous granular flow probably accommodated by diffusional mass transfer along grain boundaries of the very fine-grained syntectonic reaction products. The upper mantle was thus inferred to evolve from a high-strength layer into a low-viscosity detachment layer that accommodated significant extensional deformation within the rifted margin.
3. The transformation of granulite to eclogite also involves fracturing, fluid flux, and syntectonic reaction, and is inferred to have induced pronounced weakening and strain localization. Klaper (1990), Austrheim and Boundy (1994), and Jolivet et al. (2005) showed that during Caledonian subduction of nominally dry granulites rock in the Western Gneiss Region (Norway), metamorphic reactions were delayed until fracturing allowed fluid infiltration. The occurrence of pseudotachylites in some of these eclogitized frac-

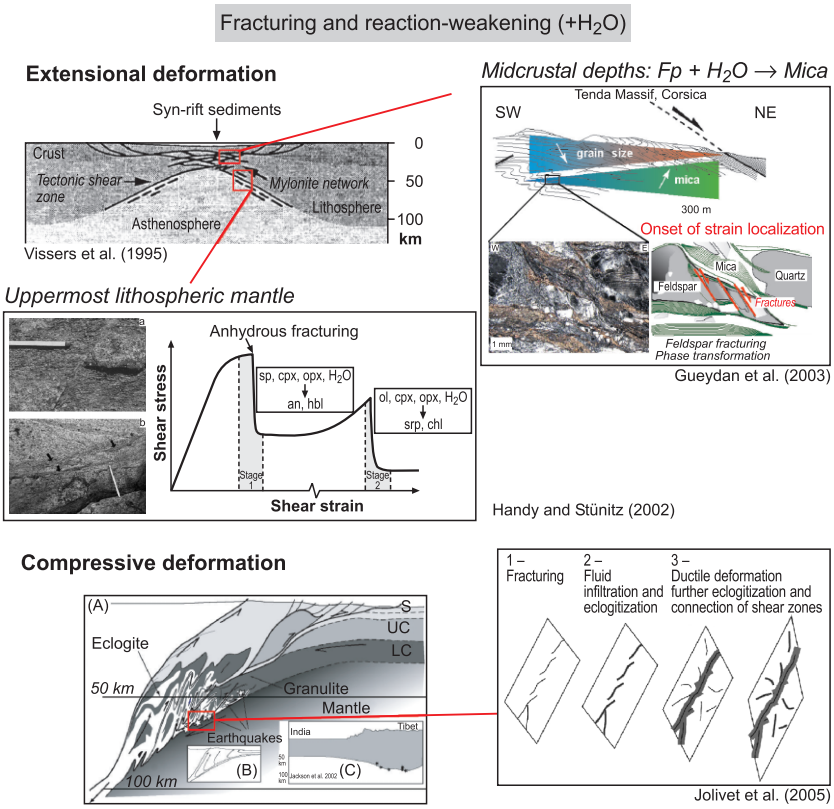

Figure 12.4 Three examples of fracturing followed by fluid influx that triggered reaction-weakening and strain localization within the lithosphere. At midcrustal depths, feldspar fracturing and reaction-softening (feldspar to mica transformation) lead to the formation of kilometer-scale extensional shear zone in the Tenda Massif, Corsica (Gueydan et al. 2003). In the uppermost mantle, fracturing and phase transformations are coeval with the formation of extensional shear zones in ultramafic rock (Handy and Stünitz 2002). Localized deformation zones (a) and (b) define a mylonitic shear zone network that accommodates extension at depths, as depicted by Vissers et al. (1995). During continental subduction (lower part), seismic fracturing of granulites followed by fluid influx and eclogitization facilitate strain localization (Austrheim and Boundy 1994; Jolivet et al. 2005). The exhumation of deep crustal units within the subduction channel may have occurred along eclogitic shear zones.

tures indicates that embrittlement was seismic and localized subsequent ductile deformation. In fact eclogitization was spurred by further deformation and fluid infiltration that resulted in the formation of isolated blocks of granulite separated by eclogitic shear zones. These blocks are inferred to have behaved like rigid inclusions between the shear zones.

Dissolution around a Fault

To accommodate large displacements, the country rock between and adjacent to faults must undergo internal deformation. This deformation is a geometrical necessity near the termination of a fault or at compressive and tensile bridges linking fault arrays. On a much smaller scale, deformation also occurs around asperities on the fault planes (Figure 12.1b). Exhumed fault segments of various seismically active faults in California reveal that pressure solution is clearly associated with fracturing through the entire thickness of the upper crust: at shallow depths, calcite is more mobile than quartz, whereas the reverse is true at greater depth (Gratier et al. 2003). These authors suggested that coseismic microfracturing enhances pressure-solution creep and may explain postseismic creep. Transient values of viscosity are expected to be high during postseismic creep; certainly greater than the mean viscosity values typical of interseismic creep (Hickman et al. 1995; Chapter 14, this volume). For example, in the same region, carbonate-rich rocks deformed at about 2 km depth within the Little Pine fault zone (California) yield strain values of 30%, and reasonable estimates of the differential stress (20 MPa) and the duration of deformation (4 Ma) indicate that the mean viscosity was about 8×10^{21} Pa s. Modeled values of effective postseismic viscosity have been evaluated assuming pressure solution of calcite in the upper part of the crust and of quartz in the lower part (see Figure 12.8f below). Postseismic viscosity is strongly dependent on the fracture density, which is not easy to evaluate. However, for a mean fracture spacing associated with each seismic episode of 200 microns, and using the creep equations above (Renard et al. 2000) the effective viscosity just after the earthquake may have been about 6×10^{18} Pa s (Gratier et al. 2003).

The evolution of viscosity is more complex as cracks and fluid advection paths evolve with time, and as fractures are progressively sealed. In fact, viscosity probably decreases exponentially with time according to the relation of Renard et al. (2000), as explained below. Strain rates in active fault zones vary due to cyclic fracturing, fluid fluxes, and reaction (Knipe and Wintsch 1985). Pressure-solution creep enhanced by microfracturing may account for some examples of aseismic displacement registered by continuously operated GPS stations arrayed on active faults (Bokelmann and Kovach 2003).

Finally, we note that dissolution in polymineralic rocks can lead to selective dissolution and removal of soluble phases, resulting in the development of tectonic layering (e.g., solution cleavage) that is initially oriented perpendicular to the direction of maximum stress (Cosgrove 1976; de Boer 1977; Robin 1978; Gratier 1987). Fletcher and Pollard (1981) have modeled this evolution as the propagation of a zone of negative dilation (a so-called “anti-crack”) around weak or depleted inclusions. The nucleation and growth of platy minerals (e.g., micas) perpendicular to the direction of maximum stress forms a schistosity. The progressive development of a mechanical anisotropy that can rotate during shearing affects the rheological and transportational properties of fault rocks.

Dissolution of Faults' Asperities

Asperities on irregular fault surfaces hinder displacement, but can also change their shape by stress-induced dissolution (Figures 12.5a, b) thereby easing deformation. In Figure 12.5d, dissolution occurs on the surface that prevents sliding (for simplicity the surface is oriented perpendicular to the maximum

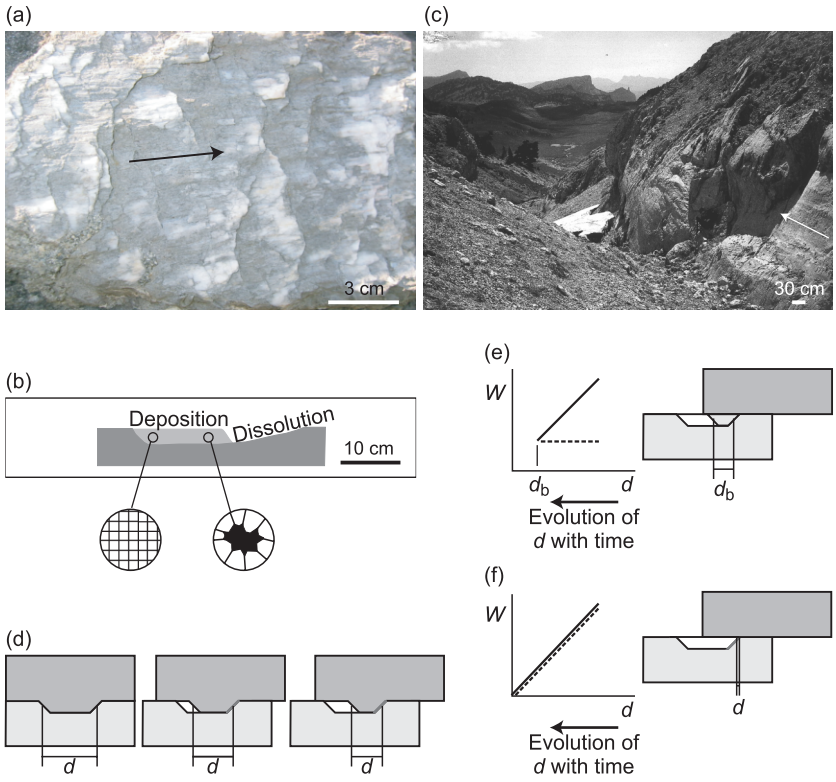

Figure 12.5 Dissolution and fracturing of asperities along a fault. (a) Mineral fibers within voids created by slow dissolution of asperities on a fault. (b) Detail of the process based on natural measurements showing the dissolution surface with directional roughness opposite to fault displacement. Mineral fibers formed by successive crack-seal events (left) attest to aseismic sliding controlled by the kinetics of pressure solution. Alternatively, cataclastic sliding was episodic, as evidenced by some large openings sealed by euhedral crystals (right). (c) Exhumed fault surface showing threading of fault parallel to fault displacement (arrows) and the various asperities at all scales. (d) Schematic evolution of dissolution deposition at the scale of a single asperity. (e) Evolution of energy (W) needed to break (continuous line) or to dissolve (dotted lines, dissolution models I or R) an asperity of decreasing size d. (f) Energy (W) needed to break (continuous line) or dissolve (dotted lines, dissolution model D) an asperity of decreasing size d. Adapted from Gratier and Gamond (1990).

stress), whereas deposition occurs in the void created by aseismic fault displacement. This in turn leads to the formation of mineral fibers on fault surfaces (Figures 12.5a, b; Gratier and Gamond 1990). The dissolution of asperities may reduce fault strength. The frictional shear strength of the fault is considered here to be the yield stress needed to fracture a large part of the fault. Its shear strength may be considered to be proportional to the cumulative length of the asperities along the fault. If the total length of asperities decreases due to their progressive dissolution, the frictional shear strength of the entire fault decreases with time. The rate of this weakening can be expressed as the relationship between the rate of dissolution and the length of the asperities, according to the theoretical relations in Eqs. 12.3–12.5 for the different rate-limiting processes. For the simple geometry adopted in Figure 12.5d, the sliding rate, d, is related to the displacement rate, $\Delta d/\Delta t$, by a numerical coefficient. In some relations (Eqs. 12.3 and 12.5), respectively, for models I and R), the sliding rate does not depend on the distance of mass transfer, d, from dissolution to deposition zones. In the other relation (Eq. 12.4, model D), the sliding rate depends on the inverse of the square of the distance of mass transfer, d. This distance, d, is the asperity length for dissolution of only one side of the fault. Because d also depends on the crystal growth mechanism, it is assumed here that each growth increment occurs at the vein-wall contact. The relation between stress and the asperity length is related to the change in energy consumed during sliding to an extent dependent on the creep law. On the other hand, the energy needed to break asperities always depends on the asperity length. Thus, the energies needed to accommodate cataclastic flow and pressure solution sliding are comparable (Figures 12.5e and 12.5f). At the scale of a single asperity, stable sliding is expected when the two energies vary similarly (e.g., pressure-solution sliding), whereas unstable sliding is expected when the two energies vary differently with successive mechanisms, thereby minimizing overall strain energy dissipation (e.g., pressure-solution sliding then cataclasis). The behavior of all asperities on a fault is more complex (Bos et al. 2000) and needs to be modeled numerically. In any case, considering all asperities, pressure solution reduces the shear strength of the fault by progressively reducing the total length of the asperities.

A main objective for future work will be to establish the geometrical evolution of asperities and their sliding mechanism (Nadeau and Johnson 1998; Sammis and Rice 1998). One way to do this is to compare the true geometry of a fault surface (Figure 12.5c) with that of threaded surfaces (Thibaut et al. 1996). A threaded surface is an uneven surface that allows the sliding of two rigid blocks without any deformation (like the surfaces of matching nuts and bolts). The deviation of real fault surfaces from that of ideally threaded surfaces may reveal the true geometry of fault asperities.

FAULT STRENGTHENING

Pervasive Strengthening

Numerous observations of natural deformation show that deposition selectively strengthens rocks. For example, quartz and calcite mineral deposits in pressure shadows of stronger minerals indent their slaty matrix by developing dissolution haloes (Figure 12.6a). Another example is "bamboo-like structures" created by boudins that selectively strengthened the boudinaged layer (Figure 12.6b). The same behavior was observed in experimentally deformed polymineralic aggregates with soluble and insoluble minerals (Zubtsov et al. 2004). At room temperature, the compaction rate of a polymineralic aggregate was significantly greater than that of a monomineralic rock comprising only a single soluble species. This may reflect the fact that the grains of monomineralic rocks grew together rather than dissolving under stress. The presence of another mineral phase favors dissolution along mutual contacts between phases with contrasting solubilities. Hickmann and Evans (1991) also found that dissolution at halite–silica interfaces (silica being insoluble) was much faster than at halite–halite interfaces, which tended to grow together. In all the natural examples (Figures 12.4 and 12.6), strengthening linked to mineral precipitation competed with weakening linked to the concentration of less-soluble micas. Deformation with mass transfer leads to a progressive segregation of rocks that induces rock heterogeneities (mass transfer from weakened zones of dissolution to strengthened zones of deposition). Therefore, rock viscosity evolves with space and time, with viscosity contrasts generally increasing to an extent dependent on the size of the closed system. The size of this closed system and the characteristic size of the induced heterogeneities mostly depend on the mechanism and scale of mass transfer: diffusion on length scales of microns to decimeters (e.g., tectonic layering) or advection on scales of hundreds to thousands of meters (e.g., ore deposits).

An atypical example where the degrees of strengthening and weakening are comparable comes from silicic volcanics of Vendée (France) affected by fluid-assisted deformation (Le Hébel et al. 2002). Deformation of the quartz-K-feldspar-phengite volcanic rock (Figure 12.6c) occurred at about 400°C and 4–5 kb. The deformation involved diffusion-driven dissolution–crystallization of quartz and feldspar, with the phengite behaving as a residual, relatively insoluble phase. Increasing strain is marked by the development of alternating mica-enriched layers (sources) and quartz-feldspar (sinks), as shown in Figure 12.6d. The former are expected to have weakened as mica content increased, whereas the latter underwent microcracking (Figure 12.6e). This process partitions strain, with very limited localization in the micaceous layers. Isotopic analysis revealed limited fluid–rock ratios, showing that the fluid originated locally and that the system remained closed during ductile deformation. No transient fluid

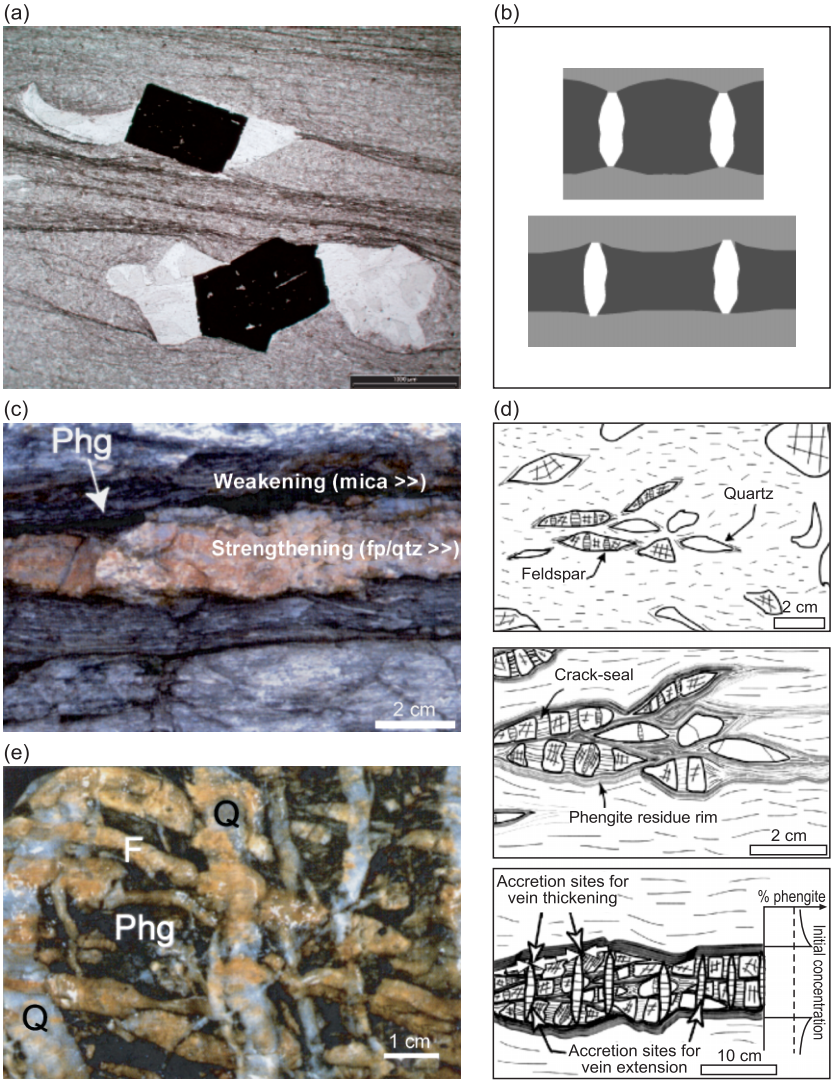

Figure 12.6 Three examples of inferred strengthening during high-strain deformation: (a) pressure shadow stronger than the slaty matrix; (b) quartz and calcite deposit between boudins (top) stronger than the boudins themselves (bottom), as sketched from a natural example. (c) to (e) Examples taken from Porphyroïds units (Vendée, France) of fluid-assisted crack-seal deformation (Le Hebel et al. 2002). (c) Porphyroïds marked by alternating quartzo-feldspathic layers rimmed by phengitic layers; (d) layering resulting from crack sealing (Le Hebel et al. 2002); pervasive fracturing of strong quartzo-feldspathic layers is coeval with dissolution of feldspar and quartz in the matrix, leading to the development of phengitic residues. K-rich fluids seal the numerous cracks, inducing growth of quartzo-feldspathic layers. (e) Detailed view of the pervasive fracturing of the quartzo-feldspathic veins.

fluxes induced by microcracking were discerned. The stability of K-feldspar is consistent with the absence of external fluids under greenschist-facies conditions. In this case, the absence of transient fluid fluxes precludes weakening at a regional scale and favors slight strengthening, as marked by numerous cracks. If the system was indeed closed, then the amount of dissolved material (quartz and K-feldspar) is equal to the amount of precipitated material.

This behavior contrasts with the large-scale evolution of zones of quartz deposition within ore deposits. Where large amounts of quartz are transported from depth by fluid flow along active faults (Sibson et al. 1988), the zone of quartz deposition appears be significantly stronger than the surrounding metamorphic country rocks.

Fault Healing and Sealing

Evidence for postseismic strength recovery comes from geophysical studies. For example, Li et al. (2003) described fault rocks from the Hector Mine rupture zone where P- and S-wave velocities increased, respectively, by 0.7%–1.4% and 0.5%–1.0% between 2000 and 2001. In contrast, velocities in surrounding rocks increased much less, indicating that the Hector Mine rupture zone healed and strengthened after the main shock, most likely as cracks that had opened during the 1999 earthquake closed up again and were sealed. The recovery of fault zone strength is consistent with a decrease in apparent crack density of 1.5% within the rupture zone. The ratio of travel time decreases for P- and S-waves was 0.72, suggesting that the cracks near the fault were partially filled with fluids. This restrengthening is similar to that observed after the 1992 M_L 7.4 Landers earthquake some 25 km to the west (Li and Vidale 2001).

The same observation can be made in experiments on faulted sandstones that were heated and subsequently re-deformed (Blanpied et al. 1995; Tenthorey et al. 2003). They show a strength recovery of 75% after 6 h of heating at 927°C. In the most extreme case, hydrothermally induced gouge compaction, cementation and crack healing resulted in 75% strength recovery after treatment at 6 h at this very high temperature. Isostatic hydrothermal treatment also resulted in dramatic reductions in porosity and permeability.

The question is thus how, and at what rate, do fractured rocks recover their strength after an earthquake? The nature of the minerals that constitute the country rocks is very important because fluid–rock interactions play a crucial role in the rheology of fault zones. We do not consider all the possibilities here, but just cite the examples of quartz and calcite, both of which are common mobile minerals in Earth's crust. The relative mobility of quartz and calcite clearly changes with depth due to differing pressure and temperature dependences of their solubilities. At shallow depths, calcite is more abundant and mobile than quartz, whereas the reverse is true at greater depth. This variation is related to two effects: first, the solubility of quartz increases with increasing temperature whereas calcite solubil-

ity decreases with increasing temperature; second, at low temperature, the kinetics of quartz dissolution is very slow, precluding significant pressure solution (Oelkers et al. 1996; Renard et al. 1997). Note that the situation is probably much more complex because temperature may have opposite effects on pressure-solution kinetics and solubility, at least in the case of calcite (Rutter 1976). Also, reaction kinetics is very sensitive to impurities in the pore fluid (Zhang et al. 2002) and this effect may outweigh the effect of temperature in nature.

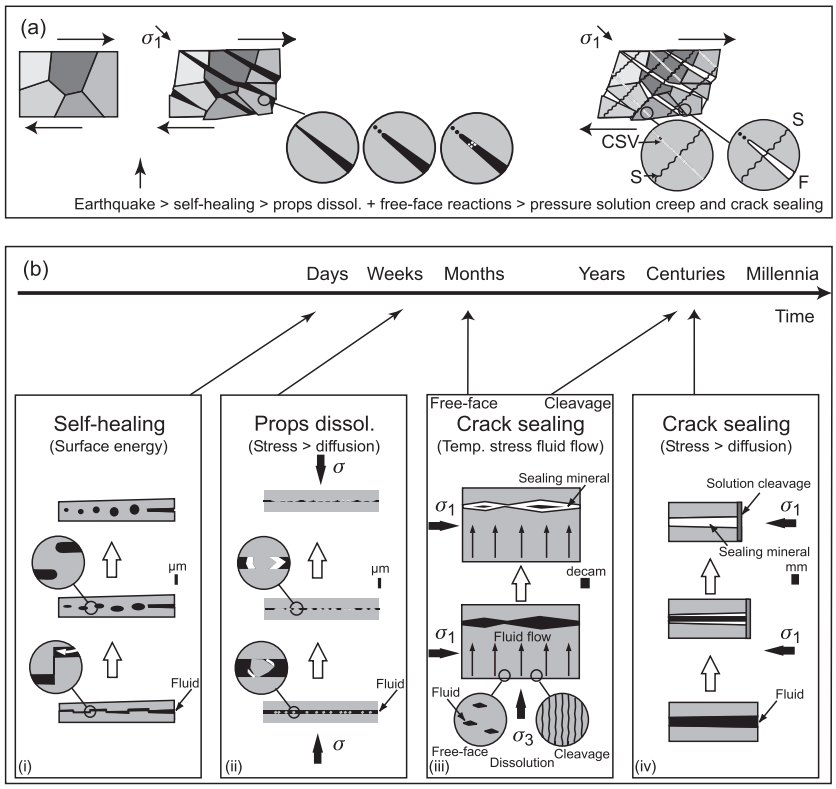

Figure 12.7 (a) Schematic view of postseismic sealing of a fault zone. The porosity (black) linked to the fracturing process is progressively sealed by a mineral deposit (white). Dissolution along stylolites or solution cleavage (S) is triggered by fracturing (F) and is associated with aseismic postseismic deformation that relaxes stress. Solution cleavage (S) and associated postseismic crack-sealed veins (CSV) also accommodate part of the strain aseismically for the duration of the interseismic period. (b) The characteristic times of sealing vary from days to millennia, with self healing driven by surface energy (i), dissolution of props driven by stress and a decrease in fluid pressure (ii), crack sealing with fluid infiltration controlled either by reactions on free faces or by diffusion along solution cleavage (iii), and crack sealing driven by stress with mass transfer from solution cleavage to fracture (iv). Figure adapted from Gratier et al. (2003).

Various mechanisms can lead to healing or sealing of rocks, as summarized in Figure 12.7. Here, we consider only the mechanisms that occur at the characteristic time of interseismic periods. Changes of fluid pressure that occur during, or just after, the main rupture with their mechanical consequences (i.e., dilational hardening, triggering of earthquakes) are discussed elsewhere (e.g., Miller 2002; Miller et al. 2003; Chapter 14, this volume).

Based on observations of natural structures (Gratier et al. 2003), the following succession of crack-sealing processes is expected in active fault zones during interseismic periods (Figure 12.7a). Initially, seismic rupture increases the overall permeability and reduces fluid pressures to near-hydrostatic values within the fault zone. This favors an increase in the reaction rates for the reasons outlined above. Self healing of the fractured minerals and some metamorphic reactions are relevant to this stage. Crack healing is driven by a decrease in microcrack surface energy (Figure 12.7b, i). No input of external material is required at this point. Solid–solid contacts are required along the fracture in order to facilitate mass transfer from sites with maximum wall curvature to sites with minimum curvature (Figure 12.7b, i). Because diffusive transfer occurs in a free (unstressed) fluid, this process is usually probably controlled by the kinetics of the interface reaction and may be rather fast (days to weeks; Brantley et al. 1990). Evidence of this process is common in naturally deformed rocks. Also relevant to this stage are free-face metamorphic reactions that are activated by the advective inflow of fluids in disequilibrium with the minerals lining the fault. This could lead either to dissolution or to deposition that is potentially rather fast (days to years) in the case of reaction on free faces around pores or voids (Figure 12.7b, iii). On the other hand, if dissolution occurs on a stressed surface, reaction kinetics is usually controlled by diffusion (i.e., sealing of large aperture cracks, Figure 12.7b, iv).

Other reactions may progress at a slower rate. Beeler and Hickman (2004) proposed that crack closure may be controlled by the dissolution of asperities and microfractured grains that prop the fracture open (Figure 12.7b, ii). This type of self-healing process is assisted by stress and requires a decrease in fluid pressure to operate effectively. A fluid pressure drop may explain the observation that dissolution pits occur in all the directions during gouge compaction (see Figure 12.8b). If this drop is sufficiently rapid, for example, during an earthquake, the rocks will tend to collapse. The experiments of Elias and Hajash (1992) in which grains or fractured rock are embedded in a "soft tube" show such pressure-solution compaction. A decrease of the compaction rate is expected with time when diffusion is rate-controlling (Figure 12.3).

The sealing of large aperture cracks (10 μm to mm–cm, Figure 12.7b, iv) combined with the large opening of the separated walls of the fracture (i.e., no contact of walls across the fracture) requires an influx of material into the cracks from outside sources. As pointed out above, long-range advective transport of dissolved solid (e.g., involving flushing by strongly oversaturated solution as

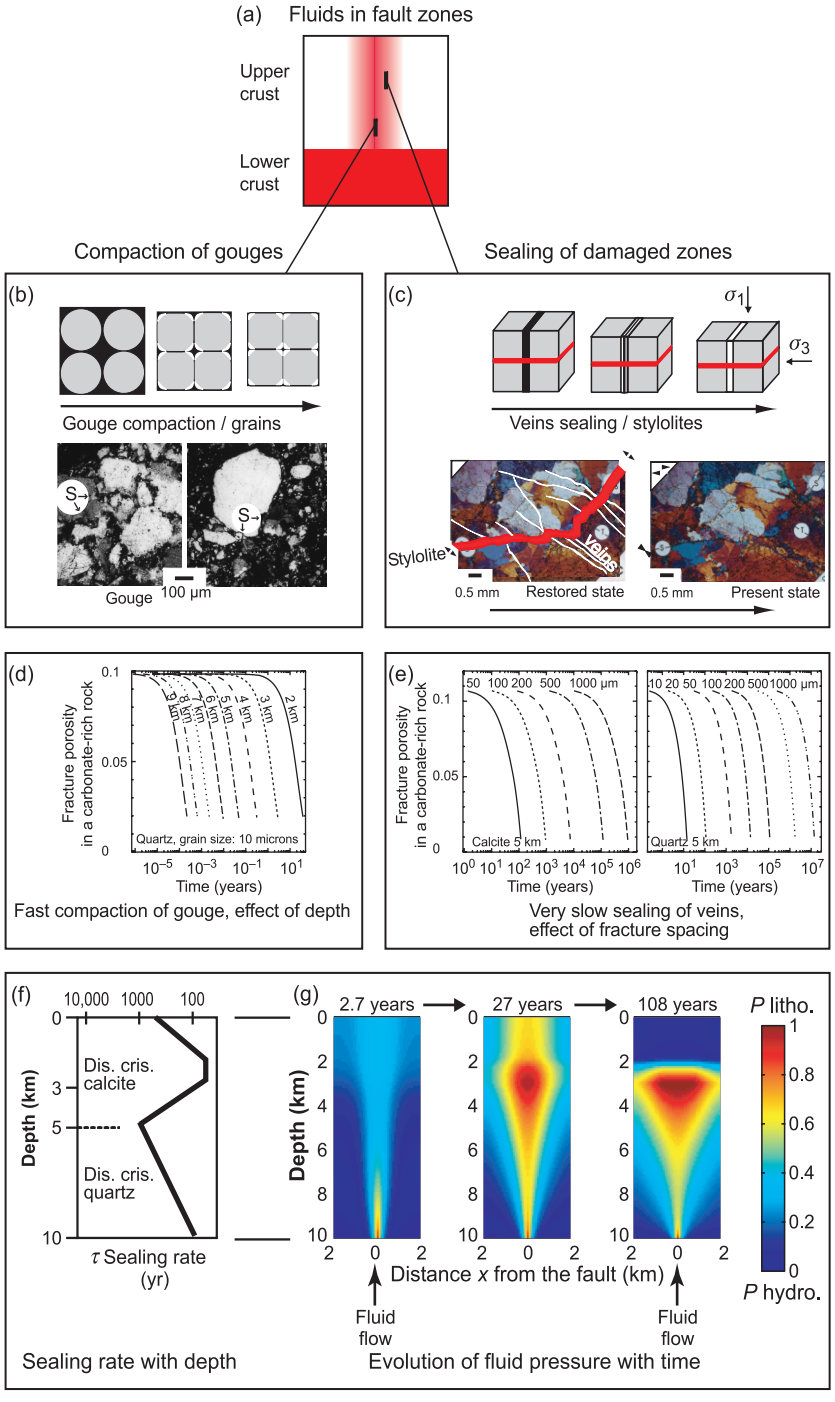
(a) Fluids in fault zones
Upper crust
Lower crust
Compaction of gouges
Sealing of damaged zones
(b)
Gouge compaction / grains
S
Gouge
100 µm
(c)
σ_1
σ_3
Veins sealing / stylolites
Stylolite
Veins
0.5 mm
Restored state
0.5 mm
Present state
(d)
Fracture porosity in a carbonate-rich rock
0.1
0.05
0
2 km
3 km
4 km
5 km
6 km
7 km
8 km
9 km
Quartz, grain size: 10 microns
10^{-5} 10^{-3} 10^{-1} 10^{1}
Time (years)
Fast compaction of gouge, effect of depth
(e)
Fracture porosity in a carbonate-rich rock
50 100 200 500 1000 µm
10 20 50 100 200 500 1000 µm
Calcite 5 km
Quartz 5 km
10^0 10^1 10^2 10^3 10^4 10^5 10^6
10^1 10^3 10^5 10^7
Time (years)
Very slow sealing of veins, effect of fracture spacing
(f)
10,000 1000 100
Depth (km)
Dis. cris. calcite
Dis. cris. quartz
τ Sealing rate (yr)
Sealing rate with depth
(g)
2.7 years
27 years
108 years
Depth (km)
Distance x from the fault (km)
Fluid flow
Fluid flow
P litho.
P hydro.
Evolution of fluid pressure with time

shown in Figure 12.7b, iii) may contribute to fracture sealing (Fyfe et al. 1978; Etheridge et al. 1984). Inflow of supersaturated fluid is documented both by stable isotopes studies (Kennedy et al. 1997) and by observations of typical mineral reactions in fault gouge (Evans and Chester 1995). This contributes to a decrease in porosity during the interseismic period, mainly in the gouge. However, it has minor effects on the sealing of nearby fractured country rocks (Gratier et al. 2003).

Following initial fast sealing (e.g., involving self-healing [Figure 12.7b, i] or by free-face metamorphic reactions [Figure 12.7b, iii]), which most often does not eliminate porosity (Figure 12.7a), crack sealing involves diffusive mass transfer (e.g., Ramsay 1980; Gratier and Gamond 1990). Mechanism of dissolution and redeposition may be recognized directly by optical microscope, by chemical analysis, or by cathodoluminescence studies. Mass transfer is proportional to the difference in chemical potential between the zones of dissolution and deposition. Most often, soluble species are removed from grain–grain contacts (stylolites, solution cleavage) and reprecipitated in veins or voids (Weyl 1959; Rutter 1976; Gratier 1987). In this case, mass transfer involves diffusion through the fluid phase trapped along the stressed contact, and can lead to the complete sealing of veins and voids (Figure 12.7b, iv, upper part). Note that solution cleavage (S) and associated postseismic crack-sealed veins (CSV, Figure 12.7a), possibly in combination with subcritical fracturing (Atkinson 1982), may accommodate part of the stress aseismically over the entire interseismic period (see also Chapter 14).

Compaction and crack sealing involves two mechanisms (Figures 12.7, 12.8): pervasive pressure solution at the grain scale in the gouge (Figure 12.8b) and vein cementation associated with dissolution along stylolites in the damaged zone around the active faults (Figure 12.8c, Gratier et al. 2003). Compaction modeling shows that these two mechanisms have different time scales (Renard et al. 2000). Pervasive pressure solution at the grain scale in fine-grained gouge is much faster than pressure solution along stylolites and associated precipitation in veins. For example, the time required to reduce permeability from 10% to near 0 at five km depth is about a month for a fine-grained quartz gouge (10 microns) and a thousand years in a damaged zone with fractures spaced 100 microns. Therefore, slow stress-driven crack sealing and compaction pro-

◂ **Figure 12.8** (a) Fluids in the upper crust rising along active faults as deduced from stable isotopes studies (Pili et al. 1998); (b) model and microstructure of gouge compaction; (c) geometry and microstructure of crack-seal veins, adapted from Gratier et al. (2003); (d) effect of depth on gouge compaction; (e) effect of fracture spacing on slow fracture sealing, adapted from Renard et al. (2000). (f) Postseismic sealing rate with depth; (g) evolution of fluid pressure within fault for predominantly calcite dissolution in the uppermost 5 km and dominantly quartz dissolution at 5 to 10 km depth, adapted from Gratier et al. (2003).

cesses control the change of porosity and permeability at depth after an earthquake. The kinetics of the sealing process during advective fluid flow may also be very slow if diffusive mass transfer of dissolved rock through the stressed intergranular fluid is the rate-limiting step (Figure 12.7b, iii, right).

Modeling of fluid transfer along active faults is possible if pressure-solution fracture sealing is combined with advective inflow of lower crust fluids (Figure 12.8a). The compaction rate in the gouge (Figure 12.8b) and the sealing rate in the damaged zone (Figure 12.8c) can be calculated (Figures 12.8d and 12.8e, respectively), the latter being the rate-controlling process (Gratier et al. 2003). The rate of sealing is modeled to decay exponentially with time. An example is given in Figure 12.8g which shows the progressive change in fluid pressure from hydrostatic (just after the earthquake) to locally near-lithostatic. Lithostatic pressure develops at two different depth intervals: at depth due to the inflow of fluid from the lower crust, and in the upper crust where calcite is available for mass transfer and relatively fast sealing of the veins (Figure 12.8f). Note that hydrothermal reactions in fault zones may lead to two competing time-dependent effects: fault strengthening due to crack sealing and fault weakening that arises from elevated pore pressures within a well-cemented, low-permeability gouge layer (Figure 12.8g).

In summary, healing and sealing processes in faults may develop over a broad range of time scales, from several days (self healing) to a thousand years (complete sealing of the veins by pressure solution and deposition). Strengthening therefore competes with weakening due to an increase in fluid pressure during progressive healing. This could help to localize the main rupture along the healed gouge and scatter the aftershocks within the strengthened, damaged fault zones. Sealing restores and even increases the cohesion of the rock. Muhuri et al. (2003) argued that sealing does not necessarily change the frictional coefficient.

A MODEL OF UPPER CRUSTAL FAULT STRENGTH

Rheological Model

As explained above, the strength of fault zones can either decrease or increase with time. The difference in the characteristic timescales of weakening and strengthening can control the rheology of active faults and thus influence the duration of seismic cycles. The simple rheological model proposed below accounts for these two effects, as shown schematically in Figure 12.9a. The fault zone is modeled here as ductile material undergoing pressure-solution creep, healing, and reaction softening. These mechanisms are assumed to operate within the seismogenic crust, as suggested by evidence for pressure solution at all depths along the San Andreas fault (Gratier et al. 2003). An alternative approach has been to model fault weakening and strengthening as due to changes in fault friction, cohesion, or pore fluid pressure (Miller 2002; Miller et al. 2003;

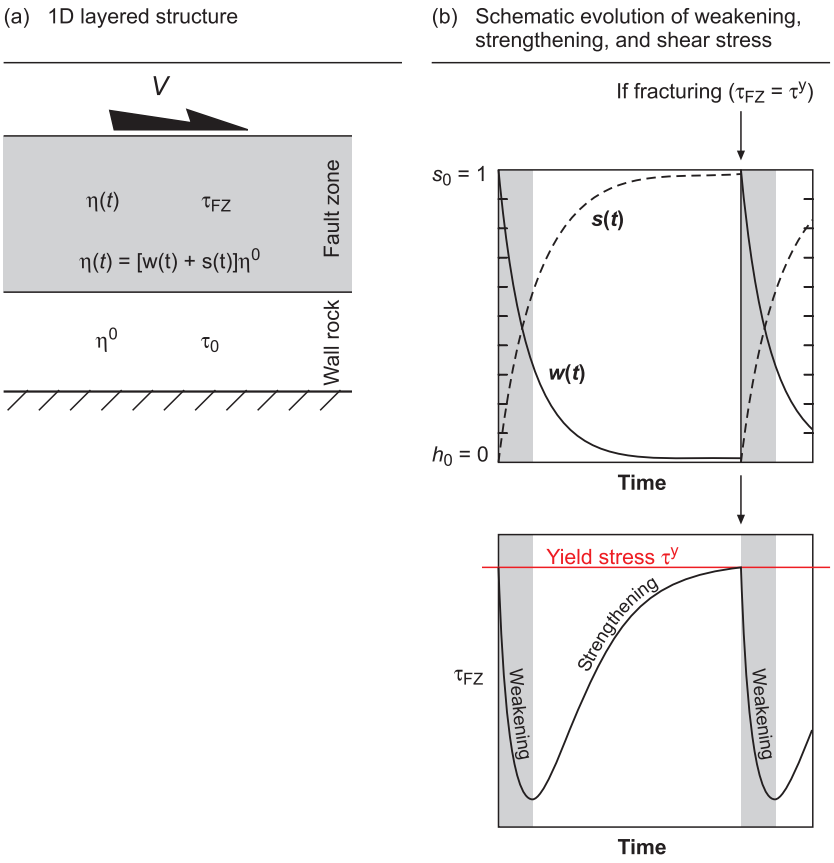

Figure 12.9 (a) Depiction of the one-dimensional-layered model of strengthening and weakening during faulting. The viscosity of the wall rock is invariant with time, while the fault zone viscosity weakens $w(t)$ and strengthens $s(t)$ with time. (b) Schematic evolution of weakening and strengthening (top) and of shear stress (bottom). Initial weakening is followed by strengthening, loading of the fault zone, leading to renewed fracturing at $\tau_{FZ} \geq \tau^y$.

Sibson and Rowland 2003). Since we are interested in quantifying the role of weakening and strengthening processes during ductile deformation, we assume that the viscosity of the fault varies with time, with respect to a constant, initial viscosity of the wall rock, η_0. Starting from this initial value, the viscosity of the fault rock, $\eta(t)$, varies with time as follows:

$$\eta(t) = [w(t) + s(t)]\,\eta_0 \quad , \text{ with } \; 0 < w(t) < 1 \; \text{ and } \; 0 < s(t) < 1 \qquad (12.6)$$

where $w(t)$ and $s(t)$ are the amounts of weakening and strengthening, respectively. The initial and final states are defined as:

Inital state: $w_0 = 1\ ,\ s_0 = 0\ ,\ \eta = \eta_0$ (12.7)

Final state: $\eta_\infty = [w_\infty + s_\infty]\eta_0$ (12.8)

The final value of weakening, w_∞, is a free parameter that is set here at $w_\infty = 10^{-2}$. The final amount of strengthening is such that $w_\infty + s_\infty = 1$ (i.e., no final change in the viscosity). s_∞ can thus be expressed as $s_\infty = 1 - w_\infty$. Note that although $w_\infty + s_\infty = 1$, $w(t) + s(t) \neq 1$ and depends on the relative amounts of weakening and strengthening. The viscosity of the fault zone thus changes with time according to relative rates of weakening and strengthening. The weakening rate, $\partial w/\partial t$, and strengthening rate, $\partial s/\partial t$, are proportional to $(w(t)–w_\infty)$ and $(s(t)–s_\infty)$, respectively. We have shown in the sections above that the strain rate, $\dot{\varepsilon}$, within the fault zone controls the rates of weakening and strengthening:

$$\frac{\partial w}{\partial t} = \varphi_w \dot{\varepsilon}[w_\infty - w(t)] \quad \text{and} \quad \frac{\partial s}{\partial t} = \varphi_s \dot{\varepsilon}[s_\infty - s(t)] \tag{12.9}$$

The scalars φ_w and φ_s define the kinetics of weakening and strengthening and are free parameters. As discussed above, weakening may be triggered by microfracturing and fluid flow, leading to post-seismic stress relaxation. Subsequent strengthening is related to interseismic sealing of these fractures. In our rheological description, initially predominant weakening yields to the following condition: $\varphi_w > \varphi_s$.

For a constant strain rate, $\dot{\varepsilon}$, the weakening and strengthening derived from Figure 12.9 become

$$\begin{aligned} w(t) &= [w_0 - w_\infty]\exp(-\varphi_w \dot{\varepsilon} t) + w_\infty \ ; \\ s(t) &= [s_0 - s_\infty]\exp(-\varphi_s \dot{\varepsilon} t) + s_\infty \quad \text{for} \quad \dot{\varepsilon} = c^{te} \ . \end{aligned} \tag{12.10}$$

The characteristic time for weakening, t_w, and strengthening, t_s, can thus be defined as

$$t_w = 1/(\varphi_w \dot{\varepsilon}) \quad \text{and} \quad t_s = 1/(\varphi_s \dot{\varepsilon}) \ . \tag{12.11}$$

Increasing φ_w at constant strain rate reduces the weakening time and leads to a sharper decrease in viscosity. An increase of strain rate (e.g., during strain localization) also enhances the viscosity reduction (decreases t_w). This corresponds to a positive feedback between weakening and strain localization. In the same way, strengthening tends to delocalize strain.

Note that at time $5t_w$, the term $\exp(-\varphi_w \dot{\varepsilon} t)$ in Eq. 12.10 is equal to 0.007, indicating that by then, weakening has almost reached its final value, s_∞. The same holds for strengthening at time $5t_s$. Weakening and strengthening thus reach their final values at the following times:

$$t_{w\,\mathrm{end}} = 5t_w = 5/(\varphi_w \dot{\varepsilon}) \quad \text{and} \quad t_{s\,\mathrm{end}} = 5t_s = 5/(\varphi_s \dot{\varepsilon}) \ . \quad (12.12)$$

After $t_{\mathrm{w\_end}}$, weakening ceases unless a new fracture resets weakening and strengthening to their initial values, as explained below. Fracturing occurs if the shear stress in the fault zone, $\tau = \eta\dot{\varepsilon} = [w(t) + s(t)]\eta_0\dot{\varepsilon}$, becomes greater than the yield stress, τ^{y}. The yield stress is assumed here to be constant, since gravity (and thus pressure) is disregarded in this study. As shown in Figure 12.8, the combined effects of advective fluid inflow and fracture sealing lead to a progressive increase of fluid pressure within the active fault, from near-hydrostatic values after an earthquake to locally overpressurized zones. Consequently, the effective shear strength of the fault is expected to decrease progressively during the interseismic period (Miller 2002; Sibson and Rowland 2003). Overall weakening of the fault zone due to the formation of gouge within a damage zone should result in a decrease of yield stress, τ^{y}, with time. We disregard this long-term evolution and focus instead on the seismic cycle computed for a constant assumed value of the yield stress, τ^{y}.

The competing effects of weakening and strengthening on the evolution of fault strength are illustrated schematically in Figure 12.9b, where strength and shear stress within the fault vary with time. After fracturing, weakening prevails and leads to a sharp decrease of fault strength. Fault strength recovers when strengthening becomes dominant, possibly leading to the seismic nucleation of new fractures.

The kinetics of the weakening and strengthening thus controls the duration of the seismic cycle, as quantified in the following section. Note that the proposed rheological model and thus the predicted duration of the seismic cycle are dimensionless. In the future, quantification of the duration of weakening and strengthening in laboratory experiments and natural slip events (e.g., coseismic and postseismic deformation measurement) could define a characteristic time for cyclical changes in fault zone rheology. This calibration could be achieved by a detailed laboratory study of the kinetics of weakening (pressure solution, reaction softening) and strengthening (healing and sealing) processes.

Boundary Conditions and Numerical Scheme

The model comprises a one-dimensional-layered medium subjected to simple shearing. The bottom of the sheared layers in Figure 12.9 is fixed, while a constant velocity, V, is imposed at the top of the layers. The constant velocity is imposed in order to determine the relative roles of weakening and strengthening in the absence of any change in loading. The average strain rate within the fault zone of width L is $\dot{\varepsilon} = V/L$. Mechanical equilibrium is attained by numerically (finite-element method) using the code SARPP (SARPP 2003). The layered structure is discretized into 100 3-noded Lagrangian elements. The velocity $v(y)$ is the only nodal unknown.

Variation in Shear Stress, Strain Rate, and Velocity

Figure 12.10 presents variations of shear stress at a given depth within the fault zone. The kinetics of weakening and strengthening were arbitrarily set at $\varphi_w = 10$ and $\varphi_s = 1$, respectively. The cyclic variations of shear stress are related to weakening (points 1 to 2) and strengthening (points 2 to 3) that prevailed in the fault zone, as discussed above. Strain rate and velocity as a function of depth within

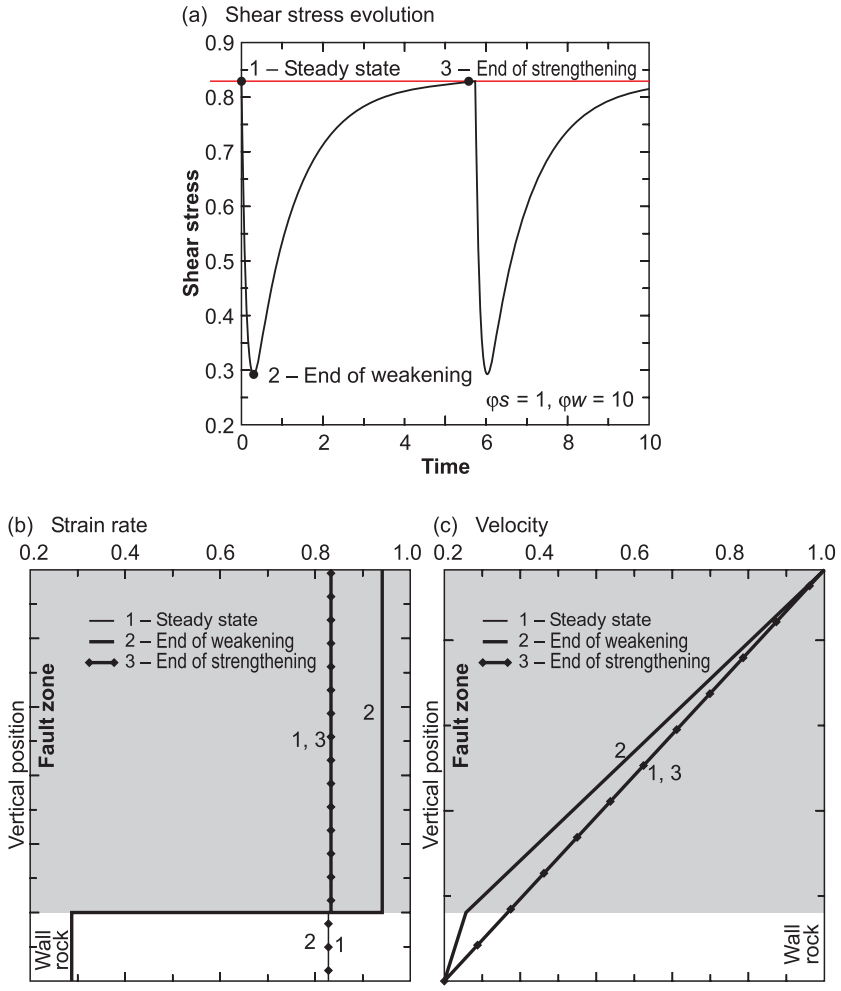

Figure 12.10 (a) Shear stress variations with time ($\varphi_s = 1$ and $\varphi_w = 10$); (b) strain rate profiles and (c) velocity profiles of the fault zone and wall rock at the beginning of the earthquake cycle (point 1: steady state in a), at the end of the weakening (point 2 in a) and at the end of strengthening (point 3 in a).

the fault are also given in Figure 12.10b and c, respectively. At the beginning of the cycle, that is, prior to the onset of weakening and strengthening, the strain rate within the fault zone and the wall rock are uniform and identical (points 1 and 3), reflecting the assumed absence of any vertical variation in the material properties of the rheological model and yielding a linear velocity profile. At the end of the weakening, the increase in strain rate of the fault is compensated by a decrease in strain rate of the wall rock in order to maintain mechanical equilibrium (uniform shear stress across the layering during simple shear). This leads to a sharp velocity gradient in the fault zone. At the end of strengthening, the strain rate in the fault zone is almost equal to the strain rate in the wall rock.

Duration of the Seismic Cycle

Figure 12.11 shows the variation of shear stress in the fault zone with time for two sets of strengthening and weakening rate constants ($\varphi_s = 1$, $\varphi_w = 10$ in curve 1 and $\varphi_s = 5$, $\varphi_w = 10$ in curve 2). The width of the fault zone, L, and the displacement velocity, V, are both set to 1, corresponding to an average strain rate of 1 ($\dot{\varepsilon} = V/L$). For $\varphi_s = 1$, $\varphi_w = 10$ (curve 1, Figure 12.11 and also Figure 12.10) a rapid decrease in shear stress is observed after the onset of fractur-

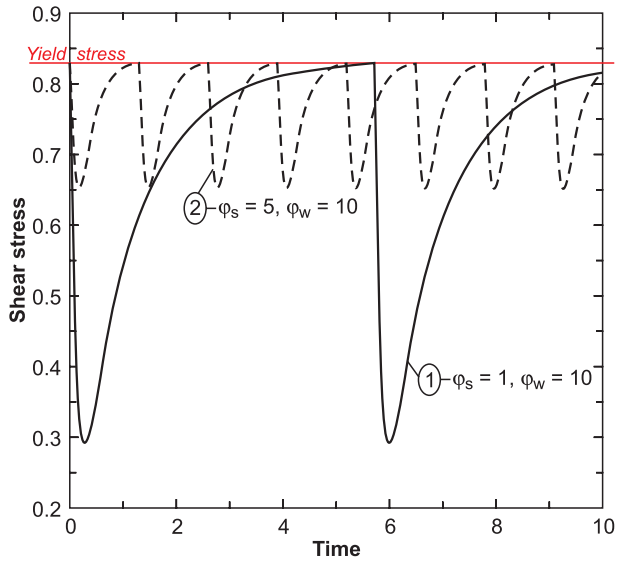

Figure 12.11 Shear stress variations with time for two rates of strengthening: $\varphi_s = 1$ (curve 1, straight line) and $\varphi_s = 5$ (curve 2, dotted line). The rate of weakening is constant at $\varphi_w = 10$ because $\varphi_w > \varphi_s$, weakening sets in immediately after fracturing at the yield stress, shown as the horizontal line. Subsequently, strengthening dominates, leading to renewed fracturing.

ing, corresponding to post-seismic stress relaxation. The duration and rate of stress decrease are governed by the rate of weakening. For $\varphi_w = 10$, the dimensionless time at the end of weakening is of the order of 0.5 (Eq. 12.12). This estimate is very close to the time when the minimum value of shear stress is attained (~0.4). Note that this time exceeds the time of the end of weakening, reflecting the positive feedback between strain localization and weakening kinetics (Eq. 12.10). During stress relaxation, strain rate increases significantly in the fault zone, leading to faster weakening. For times greater than 0.4, shear stress increases over a time whose duration is controlled by the rate of strengthening. Because this rate is an order of magnitude less than the rate of weakening, the time necessary for shear stress to increase is much greater than the time of stress relaxation. In this case, the time when strengthening ceases is of the order of 5 ($\varphi_s = 1$ and $\dot{\varepsilon} = 1$, Eq. 12.12). Again, this estimate is consistent with modeling in which strengthening ends at a time of around 6. This difference between estimated and numerical results is attributable to the decrease in bulk strain rate within the fault zone during strengthening (Figure 12.10), leading to a decrease in the rate of strengthening (Eq. 12.11). At the end of strengthening, the increase in shear stress is sufficient to trigger fracturing, which resets the weakening and strengthening variables to their initial values at the beginning of a new cycle of stress relaxation and fault loading. Since the yield stress is constant through time, the time interval between two episodes of fracturing is constant.

The time interval between two episodes of fracturing within the fault zone defines the duration of the earthquake cycle, t_{cycle}. Note again that since the proposed rheological model is dimensionless, the predicted duration of the earthquake cycle is also dimensionless. However, the real-time duration can be estimated for a natural fault if the rates of weakening and strengthening in that fault are known from creep and compaction laws. More specifically, because the earthquake cycle is defined by stress relaxation (during a time close to t_{w_end}, Eq. 12.12) and stress loading (during a time close to t_{s_end}, Eq. 12.12), the duration of the earthquake cycle is simply

$$t_{cycle} = t_{w\_end} + t_{s\_end} \approx \frac{5}{\dot{\varepsilon}}\left[\frac{1}{\varphi_w} + \frac{1}{\varphi_s}\right] . \qquad (12.13)$$

For $\varphi_s = 1$, $\varphi_w = 10$, this earthquake cycle time is about 5.1. This estimate is very close to the numerical result (curve 1, Figure 12.11). Increasing φ_s to 5 at the same φ_w (curve 2, Figure 12.11) yields a smaller earthquake cycle time ($t_{cycle} = 1.5$). Note also that this shorter cycle time coincides with a decrease in the shear stress drop during stress relaxation. This reflects the fact that increasing the strengthening rate causes strengthening to dominate the strength evolution of the fault zone earlier in the earthquake cycle. Weakening prevails during a shorter time interval, leading to less pronounced stress relaxation.

In summary, the rheology of the fault zone controls the timing of postseismic stress relaxation and interseismic stress loading. The duration of the earthquake cycle is thus controlled by the relative rates of weakening and strengthening within the fault zone. Transient weakening and strengthening are activated within the fault zone immediately after fracturing, which opens the system and induces the advective influx of fluid. Weakening is primarily related to fluid-rock interaction (reaction softening, pressure solution), whereas strengthening initiates when free fluids become rare and the fault zone is sealed.

The Role of Fault Zone Width

Figure 12.12 depicts the duration of the seismic cycle as a function of the ratio of the rates of strengthening and weakening for two values of fault zone width, $L = 1$ and $L = 10$. Increasing the width of the fault zone from 1 to 10 leads to a corresponding, order-of-magnitude increased in the cycle duration. Therefore, an increase of L at constant displacement velocity, V, involves a decrease in strain rate and an increase in the duration of the earthquake cycle (Eq. 12.13). If we assume that the width of the fault zone is related to its length, these results indicate that the seismic cycle of a large fault is much longer than that of a minor fault, as observed in nature.

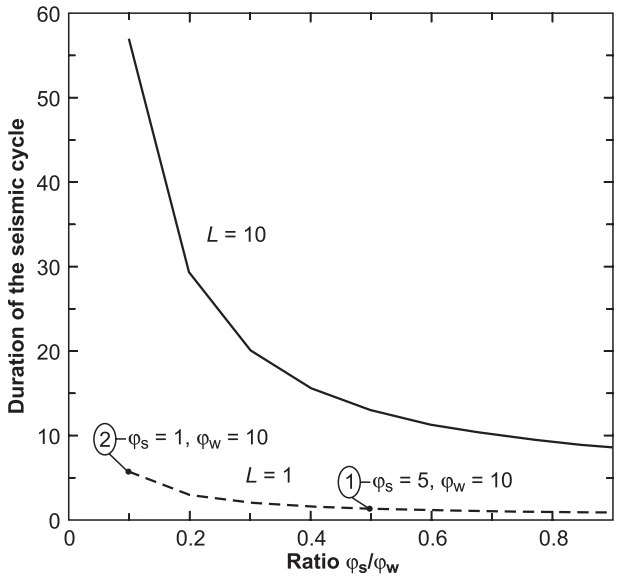

Figure 12.12 Duration of the earthquake cycle as a function of the ratio of strengthening to weakening rates for two values of fault zone width, $L = 1$ and 10. Points 1 and 2 refer to numerical simulation of Figure 12.10 for $L = 1$.

Concluding remarks

Within upper crustal faults, the interaction of fracturing, pressure solution, and mineral reactions leads to unstable deformation, characterized by fast, episodic slip alternating with slow creep. At the time scale of the earthquake cycle, fracturing speeds up the kinetics of pressure solution and reaction, thereby weakening the fault, whereas healing and sealing of fractures re-strengthen the fault zone. These mechanisms also relax stress during the interseismic period and partly smooth asperities on fault surfaces. The effect of fracturing on the dissolution process is faster than healing and sealing of the fault, such that weakening predominates just after earthquake whereas strengthening occurs more progressively with time. Strengthening associated with fault sealing is sometimes counteracted by weakening related to a decrease in permeability and—given sufficient fluid inflow—to an increase in pore-fluid pressure in the fault zone. Numerical modeling indicates that the relative rates of weakening and strengthening control the temporal evolution of fault strength during the interseismic period, and thus the duration of the earthquake cycle.

Future Research

Microstructural Approach

Numerous parameters control the characteristic times of mechanical and physical responses to seismic events. The kinetics of weakening- and strengthening processes are, of course, key factors in this response. As presented in this chapter, different creep and compaction laws are possible depending on the parameters used (see also Chapter 7). Further experiments are required to constrain these parameters, as well as to establish the rate-limiting steps of the weakening and strengthening processes. A vexing problem is that the processes examined in nature operate on time scales that far exceed the average human life span.

Another major parameter that can only be inferred from the detailed analysis of natural fault zones is the relative contributions of advective and diffusive modes of mass transport. Closely related to this is the mean distance of mass transfer within fluids (see also Chapter 11). Careful microstructural and geochemical analysis of naturally deformed rock is required to establish this distance, which can range from the spacing between fractures in a rock with solution cleavage (diffusive mass transfer) to thousands meters in veined rocks (advective transport).

Multiscaling Approach

We understand how individual asperities on a fault are dissolved or broken, but determining the bulk effect of asperities at all scales on macroscopic fault behavior is a true challenge. A first step will be to evaluate the geometry of the

asperities on exhumed fault surfaces and to consider asperities at all scales as deviations from the ideal model of a threaded surface. Also needed for quantitative models are the scaling properties of fractures (their width, length, and spacing), as these are expected to play a key role in weakening and strengthening.

Macrostructural Approach

Testing models requires in-depth studies of real faults. Measurements of how mechanical and physical properties of faults zone evolve during the interseismic period are, of course, very important. In particular, monitoring fluid pressure could be combined with geodetic measurements of fault motion (see Chapter 4) to establish the relationship between fault displacement and fluid pressure evolution along active faults. This would be especially interesting to do immediately after earthquakes, in order to capture the postseismic creep triggered by fracturing, then the expected links between postseismic strengthening and the recovery of high fluid pressure. Finite displacements during aftershocks can be regarded in the broader context of long-term displacements obtained with geodetic measurements in order to constrain the postseismic creep rate and the strain localization along active fault zones. Fault zones with a regular earthquake recurrence time and constant displacement rate (e.g., Parkfield, southern California) lend themselves well to this kind of study, because they are expected to show features that are diagnostic of recurrent, competitive weakening and strengthening during the interseismic period.

Finally, the idea that inherited and induced heterogeneities on several length scales can trigger instabilities introduces the notion of self-organized complexity that prevents us from accurate prediction of earthquakes on useful time and length scales (days to months, meters to kilometers). Earthquake predictions are, and will remain, beset with large uncertainties. Evaluating these uncertainties remains a challenge that can only be met by the careful study of structural heterogeneities and their effects on self-organization.

Numerical Modeling

Future modeling should account not only for changes of fault zone rheology during the earthquake cycle as proposed in this chapter, but also for changes of pore fluid pressure. Following an earthquake, the combined effect of advective fluid inflow and fracture sealing in the fault core could lead to an increase of fluid pressure from near-hydrostatic after the earthquake to locally overpressurized, at least along some parts of the fault (see Chapter 14 for a discussion of postseismic pore-fluid pressure evolution). Consequently, both the yield strength and effective shear strength of a fault could decrease with time during the interseismic period, particularly if a gouge develops. Therefore, an important step will be to incorporate transient yield stress into models of the seismic cycle.

ACKNOWLEDGEMENTS

We thank D. Gapais for his detailed comments on a previous version of the manuscript and C. Spiers, M. Handy, and J. Urai for their very helpful reviews of the final version. We also thank P. Labaume, P. Vialon, and A.-M. Boullier, respectively, for the photographs in Figures 12.3d, 12.5c, and 12.6a.

REFERENCES

Atkinson, B.K. 1982. Subcritical crack propagation in rocks: Theory, experimental results, and applications. *J. Struct. Geol.* **4**:41–56.

Austrheim, H., and T. Boundy. 1994. Pseudotachylites generated during seismic faulting and eclogitization of the deep crust. *Science* **265**:82–83.

Beeler, N.M., and S.H. Hickman. 2004. Stress-induced, time-dependent fracture closure at hydrothermal conditions. *J. Geophys. Res.* **109**:1–16.

Blanpied, M.L., D.A. Lockner, and J.D. Byerlee. 1995. Frictional slip of granite at hydrothermal conditions. *J. Geophys. Res.* **100**:13,045–13,064.

Bokelmann, G.H.R., and R. Kovach. 2003. Long-term creep rate changes and their causes. *Geophys. Res. Lett.* **30**:NIL_9-NIL_12.

Bos, B., C.J. Peach, and C.J. Spiers. 2000. Frictional-viscous flow of simulated fault gouge caused by the combined effects of phyllosilicates and pressure solution. *Tectonophysics* **327**:173–194.

Brantley, S., B. Evans, S.H. Hickman, and D.A. Crerar. 1990. Healing of microcracks in quartz: Implications for fluid flow. *Geology* **18**:136–139.

Cosgrove, J.W. 1976. The formation of crenulation cleavage. *J. Geol. Soc. Lond.* **132**:155–178.

De Boer, R.B., P.J.C. Nagtegaal, and E.M. Duyvus. 1977. Pressure solution experiment on quartz sand. *Geochim. Cosmochim. Acta* **41**:257–264.

de-Meer, S., C.J. Spiers, C.J. Peach, and T. Watanabe. 2002. Diffusive properties of fluid-filled grain boundaries measured electrically during active pressure solution. *Earth Planet. Sci. Lett.* **200**:147–157.

den Brok, S.B. 1998. Effect of microcracking on pressure solution strain rate: The Gratz grain boundary model. *Geology* **26**:915–918.

Dewers, T., and P. Ortoleva. 1990. A coupled reaction/transport/mechanical model for intergranular pressure solution stylolites, and differential compaction and cementation in clean sandstones. *Geochim. Cosmochim. Acta* **54**:1609–1625.

Dixon, J., and G. Williams. 1983. Reaction softening in mylonites from the Arnaboll thrust, Sutherland. *Scott. J. Geol.* **19**:157–168.

Dysthe, D.K., F. Renard, J. Feder et al. 2003. High-resolution measurements of pressure solution creep. *Phys. Rev. E* **6801**:317–329.

Elias, B.P., and A. Hajash. 1992. Changes in quartz solubility and porosity due to effective stress: An experimental investigation of pressure solution. *Geology* **20**:451–454.

Etheridge, M.A., S.F. Cox, V.J. Wall, and R.H. Vernon. 1984. High fluid pressures during regional metamorphism and deformation: Implications for mass transfer and deformation mechanisms. *J. Geophys. Res.* **89**:4344–4558.

Evans, J.P., and F.M. Chester. 1995. Fluid–rock interaction in faults of the San Andreas system: Inferences from the San Gabriel fault rock geochemistry. *J. Geophys. Res.* **100**:13,007–13,020.

Farver, J.R., and R.A. Yund. 1998. Oxygen grain boundary diffusion in natural and hot-pressed calcite aggregates. *Earth Planet. Sci. Lett.* **161**:189–200.

FitzGerald, J.D., and H. Stünitz. 1993. Deformation of granitoids at low metamorphic grade. I: Reactions and grain size reduction. *Tectonophysics* **221**:269–297.

Fletcher, R.C., and D.D. Pollard. 1981. Anticrack model for pressure solution surfaces. *Geology* **9**:419–424.

Fyfe, W.S., N.J. Price, and A.B. Thomson. 1978. Fluids in the Earth's Crust. Developments in Geochemistry I. Amsterdam: Elsevier.

Gapais, D. 1989. Shear structures within deformed granites: Mechanical and thermal indicators. *Geology* **17**:1144–1147.

Gibbs, J.W. 1877. On the equilibrium of heterogeneous substances. *Trans. Connecticut Acad.* **3**:108–248; 343–524.

Gratier, J.P. 1987. Pressure solution-deposition creep and associated tectonic differentiation in sedimentary rocks. In: Deformation of Sediments and Sedimentary Rocks, ed. M.E. Jones and R.M.F. Preston, Spec. Publ. 29, pp. 25–38. London: Geol. Soc.

Gratier, J.P., P. Favreau, and F. Renard. 2003. Modeling fluid transfer along California faults when integrating pressure solution crack sealing and compaction processes. *J. Geophys. Res.* **108**:B2, 28–52.

Gratier, J.P., and J.F. Gamond. 1990. Transition between seismic and aseismic deformation in the upper crust. In: Deformation Mechanisms, Rheology and Tectonics, ed. R.J. Knipe and E.H. Rutter, Spec. Publ. 54, pp. 461–473. London: Geol. Soc.

Gratier, J.P., F. Renard, and P. Labaume. 1999. How pressure solution and fractures interact in the upper crust to make it behave in both a brittle and viscous manner. *J. Struct. Geol.* **21**:1189–1197.

Gratz, A.J. 1991. Solution-transfer compaction of quartzites: Progress toward a rate law. *Geology* **19**:901–904.

Gueydan, F., Y.M. Leroy, L. Jolivet, and P. Agard. 2003. Analysis of continental midcrustal strain localization induced by reaction softening and microfracturing. *J. Geophys. Res.* **108**:B2, 2064, doi:10.1029/2001JB000611.

Handy, M.R. 1989. Deformation regime and the rheological evolution of fault zones in the lithosphere. The effect of pressure, temperature, grain size and time. *Tectonophysics* **163**:119–159.

Handy, M.R., and H. Stünitz. 2002. Strain localization by fracturing and reaction weakening: A mechanism for initiating exhumation of subcontinental mantle beneath rifted margins. In: Deformation Mechanisms, Rheology and Tectonics: Current Status and Future Perspectives, ed. S. de Meer, M.R. Drury, J.H.P. de Bresser, and J.M. Pennock, Spec. Publ. 200, pp. 387–407. London: Geol. Soc.

Hickman, S.H., and B. Evans. 1991. Experimental pressure solution in halite: The effect of grain–interphase boundary structure. *J. Geol. Soc. Lond.* **148**:549–560.

Hickman, S.H., and B. Evans. 1995. Kinetics of pressure solution at halite–silica interfaces and intergranular clay films. *J. Geophys. Res.* **100**:B7, 13,113–13,132.

Hickman, S., R.H. Sibson, and R. Bruhn. 1995. Introduction to special section: Mechanical involvement of fluids in faulting. *J. Geophys. Res.***100**:B7, 12,831–12,840.

Hilgers, C., K. Dilg-Gruschinski, and J.L. Urai. 2004. Microstructural evolution of syntaxial veins formed by advective flow. *Geology* **32**:261–264.

Jolivet, L., H. Raimbourg, L. Labrousse et al. 2005. Softening triggered by eclogitization: The first step toward exhumation during continental subduction. *Earth Planet. Sci. Lett.* **237**:532–547.

Kennedy, B.M., Y.K. Kharaka, W.C. Evans et al. 1997. Mantle fluids in the San Andreas fault system, California. *Science* **278**:1278–1280.

Kingery, W.D., H.K. Bowen, and D.R. Uhlmann. 1976. Introduction to Ceramics. New York: Wiley.

Klaper, E.M. 1990. Reaction-enhanced formation of eclogite-facies shear zones in granulite-facies anorthosites. In: Deformation Mechanisms, Rheology and Tectonics, ed. R.J. Knipe and E.H. Rutter, Spec. Publ. 54, pp. 167–174. London: Geol. Soc.

Knipe, R.J., and R.P. Wintsch. 1985. Heterogeneous deformation, foliation development, and metamorphic processes in a polyphase mylonite. In: Metamorphic Reactions: Kinetics, Textures, and Deformation, A.B. Thompson and D.C. Rubie, pp. 180–210. Berlin: Springer.

Le Hebel, F., D. Gapais, S. Fourcade, and R. Capdevila. 2002. Fluid-assisted large strains in a crustal-scale décollement (Hercynian Belt of South Brittany, France). In: Deformation Mechanisms, Rheology and Tectonics: Current Status and Future Perspectives, ed. S. de Meer, M.R. Drury, J.H.P. de Bresser, and J.M. Pennock, Spec. Publ. 200, pp. 85–101. London: Geol. Soc.

Lehner, F.K. 1995. A model for intergranular pressure solution in open systems. *Tectonophysics* **245**:153–170.

Li, Y.G., and J.E. Vidale. 2001. Healing of the shallow fault zone from 1994–1998 after the 1992 *M* 7.5 Landers, California, earthquake. *Geophys. Res. Lett.* **28**: 2999–3002.

Li, Y.G., J.E. Vidale, S.M. Day, D.D. Oglesby, and E. Cochran. 2003. Postseismic fault healing on the rupture zone of the 1999 *M* 7.1 Hector Mine, California, earthquake. *Bull. Seismol. Soc. Am.* **93**:854–869.

McEwen, T.J. 1978. Diffusional mass transfer processes in pitted pebble conglomerates. *Contrib. Mineral. Petrol.* **67**:405–415.

Means, W.D., and T. Li. 2001. A laboratory simulation of fibrous veins: Some first observations. *J. Struct. Geol.* **23**: 857–863.

Miller, S.A. 2002. Properties of large ruptures and the dynamical influence of fluids on earthquakes and faulting, *J. Geophys. Res.* **107**:536–548.

Miller, S.A., W. van-der-Zee, D.L. Olgaard, and J.A.D. Connolly. 2003. A fluid pressure feedback model of dehydration reactions: Experiments, modeling, and application to subduction zones. *Tectonophysics* **370**:241–251.

Mitra, G. 1978. Ductile deformation zones and mylonites: The mechanical process involved in the deformation of crystalline basement rocks. *Am. J. Sci.* **278**: 1057–1084.

Muhuri, S.K., T.A. Dewers, G.E. Scott, and Z. Reches. 2003. Interseismic fault strengthening and earthquake-slip instability: Friction or cohesion? *Geology* **31**:881–884.

Muller, W., D. Aerden, and A.N. Halliday. 2000. Isotopic dating of strain fringe increments: Duration and rates of deformation in shear zones. *Science* **288**:2195–2197.

Nadeau, R.M., and L.R. Johnson. 1998. Seismological studies at Parkfield VI: Moment release rates and estimates of source parameters for small repeating earthquakes. *Bull. Seismol. Soc. Am.* **88**:790–814.

Niemeijer, A.R., and C.J. Spiers. 2002. Compaction creep of quartz sand at 400–600°C: Experimental evidence for dissolution-controlled pressure solution. *Earth Planet. Sci. Lett.* **195**:261–273.

Oelkers, E.H., P.A. Bjørkum, and W.M. Murphy. 1996. A petrographic and computational investigation of quartz cementation and porosity reduction in North Sea sandstones. *Am. J. Sci.* **296**:420–452.

Paterson, M.S. 1973. Nonhydrostatic thermodynamics and its geologic applications. *Rev. Geophys. & Space Phys.* **11**:355–389.

Paterson, M.S. 2001. Relating experimental and geological rheology. *Intl. J. Earth Sci. (Geol. Rundsch.)* **90**:157–167.

Pfiffner, O.A., and J.G. Ramsay. 1982. Constraints on geological rate: Arguments from finite strain values of naturally deformed rocks. *J. Geophys. Res.* **87**:311–321.

Pili, E.B., B.M. Kennedy, M.S. Conrad, and J.P. Gratier. 1998. Isotope constraints on the involvement of fluids in the San Andreas fault. *EOS Trans. AGU* **79**:S229–S320, Spring meeting

Raj, R. 1982. Creep in polycrystalline aggregates by matter transport through a liquid phase. *J. Geophys. Res.* **87**:4731–4739.

Ramsay, J.G. 1980. The crack-seal mechanism of rock deformation. *Nature* **284**:135–139.

Renard, F., A. Park, J.P. Gratier, and P. Ortoleva. 1997. An integrated model for transitional pressure solution in sandstone. *Tectonophysics* **312**:97–115.

Renard, F., J.P. Gratier, and B. Jamtveit. 2000. Kinetics of crack-sealing, intergranular pressure solution, and compaction around active faults. *J. Struct. Geol.* **22**:1395–1407.

Robin, P.Y. 1978. Pressure solution at grain-to-grain contacts. *Geochim. Cosmochim. Acta* **42**:1383–1389.

Robin, P.Y. 1979. Theory of metamorphic segregation and related processes. *Geochim. Cosmochim. Acta* **43**:1587–1600.

Rutter, E.H. 1976. The kinetics of rock deformation by pressure solution. *Phil. Trans. R. Soc. Lond.* **283**:203–219.

Rutter, E.H. 1983. Pressure solution in nature, theory, and experiment. *J. Geol. Soc. Lond.* **140**:725–740.

Sammis, G.C., and J.R. Rice. 1998. Repeating earthquakes as low-stress-drop events at a border between locked and creeping fault patches. *Bull. Seismol. Soc. Am.* **91**: 532–537.

SARPP. 2003. Structural Analysis and Rock Physics Program, Y.M. Leroy and F. Gueydan, LMS, Ecole Polytechnique, Palaiseau, France.

Shimizu, I. 1995. Kinetics of pressure solution creep in quartz: Theoretical considerations. *Tectonophysics* **245**:121–134.

Sibson, R.H., F. Robert, and H.H.A.F. Poulsen. 1988. High angle faults, fluid pressure cycling, and mesothermal gold-quartz deposits. *Geology* **16**:551–555.

Sibson, R.H., and J.V. Rowland. 2003. Stress, fluid pressure, and structural permeability in seismogenic crust, North Island, New Zealand. *Geophys. J. Intl.* **154**:584–594.

Simpson, C. 1985. Deformation of granitic rocks across the brittle–ductile transition. *J. Struct. Geol.* **7**:503–511.

Sorby, H.C. 1865. On impressed limestone pebbles, as illustrating a new principle in chemical geology. *Proc. West Yorks. Geol. Soc.* **14**:458–461.

Spiers, C.J., and P.M. Schutjens. 1990. Densification of crystalline aggregates by fluid phase diffusional creep. In: Deformation Processes in Minerals, Ceramics, and Rocks, ed. D.J. Barber and P.G. Meredith, pp. 334–353. London: Unwin Hyman.

Stel, H. 1981. Crystal growth in cataclasites: Diagnostic microstructures and implications. *Tectonophysics* **78**:585–600.

Taber, S. 1916. The growth of crystals under external pressure. *Am. J. Sci.* XLI (4th series) **246**:532–556.

Tada, R., and R. Siever. 1986. Experimental knife-edge pressure solution of halite. *Geochim. Cosmochim. Acta* **50**:29–36.

Tenthorey, E., S.F. Cox, and H.F. Todd. 2003. Evolution of strength recovery and permeability during fluid–rock reaction in experimental fault zones. *Earth Planet. Sci. Lett.* **206**:161–172.

Thibaut, M., J.P. Gratier, M. Léger, and J.M. Morvan. 1996. An inverse method for determining three-dimensional fault geometry with thread criterion: Application to strike-slip and thrust faults (Western Alps and California). *J. Struct. Geol.* **18**:1127–1138.

Vissers, R.L.M., J.P. Platt, and D. van der Wal. 1995. Late orogenic extension of the Betic Cordillera and the Alboran Domain: A lithospheric view. *Tectonics* **14**:786–803.

Weyl, P.K. 1959. Pressure solution and the force of crystallization: A phenomenological theory. *J. Geophys. Res.* **64**:2001–2025.

White, S.H., and R.J. Knipe. 1978. Transformation and reaction-enhanced ductility in rocks. *J. Geol. Soc. Lond.* **135**:513–516.

Wibberley, C.A.J. 1999. Are feldspar-to-mica reactions necessarily reaction-softening processes in fault zones? *J. Struct. Geol.* **21**:1219–1227.

Wintsch, R.P., R. Christoffersen, and A.K. Kronenberg. 1995. Fluid–rock reaction weakening in fault zones. *J. Geophys. Res.* **100**:13,021–13,032.

Zhang, X., J. Salemans, C.J. Peach, and C.J. Spizers. 2002. Compaction experiments on wet calcite powder at room temperature: Evidence for operation of intergranular pressure solution. In: Deformation Mechanisms, Rheology and Tectonics: Current Status and Future Perspectives, ed. S. de Meer, M.R. Drury, J.H.P. de Bresser, and J.M. Pennock, Spec. Publ. 200, pp. 29–40. London: Geol. Soc.

Zubtsov, S.F., F. Renard, J.P. Gratier et al. 2004. Experimental pressure solution creep of polymineralic aggregates. *Tectonophysics* **385**:45–47.